Title: Circuit and synaptic organization of forebrain-to-midbrain pathways that promote and suppress vocalization

Running title: Inhibitory neurons push and pull the midbrain USV circuit

Valerie Michael[1], Jack Goffinet[1], John Pearson[1, 2], Fan Wang[1], Katherine Tschida[3*], Richard Mooney[1*]

[1]Department of Neurobiology, Duke University Medical Center, Durham, NC 27710

[2]Department of Biostatistics & Bioinformatics, Duke University Medical Center, Durham, NC 27710

[3]Department of Psychology, Cornell University, Ithaca, NY 14853

[*]Co-corresponding authors: Katherine Tschida, email: kat227@cornell.edu; Richard Mooney, email: mooney@neuro.duke.edu

Abstract

Animals vocalize only in certain behavioral contexts, but the circuits and synapses through which forebrain neurons trigger or suppress vocalization remain unknown. Here we used transsynaptic tracing to identify two populations of inhibitory neurons that lie upstream of neurons in the periaqueductal gray that gate the production of ultrasonic vocalizations in mice (i.e., PAG-USV neurons). Activating PAG-projecting neurons in the preoptic hypothalamus (POA_{PAG} neurons) elicited USV production in the absence of social cues. In contrast, activating PAG-projecting neurons in the central-medial boundary zone of the amygdala ($Amg_{C/M\text{-}PAG}$ neurons) transiently suppressed USV production without disrupting non-vocal social behavior. Optogenetics-assisted circuit mapping in brain slices revealed that POA_{PAG} neurons directly inhibit PAG interneurons, which in turn inhibit PAG-USV neurons, whereas $Amg_{C/M\text{-}PAG}$ neurons directly inhibit PAG-USV neurons. These experiments identify two major forebrain inputs to the PAG that trigger and suppress vocalization, respectively, while also establishing the synaptic mechanisms through which these neurons exert opposing behavioral effects.

Keywords: vocalization, ultrasonic, preoptic, hypothalamus, amygdala, periaqueductal gray

Introduction

The decision to vocalize is often a matter of life and death, as vocalizations are an important medium for sexual and social signaling between conspecifics but may also inadvertently advertise the caller's location to eavesdropping predators. Consequently, many factors influence the decision to vocalize, including the presence of external sensory and social cues, as well as the animal's own internal state and past experience. Work from the last five decades has established the midbrain periaqueductal gray (PAG) as an obligatory gate for the production of vocalizations in all mammals (Fenzl and Schuller, 2002; Jurgens, 1994, 2002, 2009; Subramanian et al., 2020; Sugiyama et al., 2010; Tschida, 2019), and it is thought that forebrain inputs to the PAG regulate the production of vocalizations in a context-dependent fashion. In line with this idea, forebrain regions including the cortex, amygdala, and hypothalamus have been implicated in regulating vocalization as a function of social context (Bennett et al., 2019; Dujardin and Jurgens, 2006; Gao et al., 2019; Green et al., 2018; Jurgens, 1982, 2002; Kyuhou and Gemba, 1998; Ma and Kanwal, 2014; Manteuffel et al., 2007). Notably, although electrical or pharmacological activation of various forebrain regions can elicit vocalizations (Jurgens, 2009; Jurgens and Ploog, 1970; Jurgens and Richter, 1986), these effects depend on an intact PAG (Jurgens and Pratt, 1979; Lu and Jurgens, 1993; Siebert and Jurgens, 2003), suggesting that the PAG acts as an essential hub for descending forebrain control of vocalization. Despite the centrality of the PAG to vocalization, the synaptic mechanisms through which forebrain neurons interact with the PAG vocal gating circuit to either promote or suppress vocalization remain unknown.

A major challenge to understanding the synaptic mechanisms through which descending forebrain neurons influence vocalization was that, until recently, the identity of the PAG neurons that play an obligatory role in vocal gating remained unknown. The PAG is a functionally heterogeneous structure important to many survival behaviors (Bandler and Shipley, 1994;

Carrive, 1993; Evans et al., 2018; Holstege, 2014; Tovote et al., 2016), thus hindering the identification of vocalization-related PAG neurons and forebrain inputs to these neurons that might influence vocalization. To overcome this challenge, we recently used an intersectional activity-dependent genetic tagging technique to identify neurons in the PAG of the mouse that gate the production of ultrasonic vocalizations (USVs) (i.e., PAG-USV neurons (Tschida et al., 2019)), which mice produce in a variety of social contexts (Chabout et al., 2015; Holy and Guo, 2005; Maggio and Whitney, 1985; Neunuebel et al., 2015; Nyby et al., 1979; Portfors and Perkel, 2014; Whitney et al., 1974). The identification of PAG-USV neurons opens the door to identifying their monosynaptic inputs and to understanding how these afferent synapses modulate neural activity within the PAG vocal gating circuit to influence vocal behavior.

Here we combined intersectional methods and transsynaptic tracing to identify neurons that provide monosynaptic input to PAG-USV neurons and to local PAG inhibitory interneurons. Using this transsynaptic tracing as an entry point, we then identified inhibitory neurons in both the hypothalamus and the amygdala that provide synaptic input to the PAG vocal gating circuit. In male and female mice, we found that optogenetic stimulation of hypothalamic afferents to the PAG-USV circuit promoted USV production in the absence of any social cues, whereas similar stimulation of amygdalar afferents to the PAG-USV circuit in males suppressed spontaneous USV production elicited by social encounters with females. Lastly, we used optogenetic assisted circuit mapping in brain slices to deduce the synaptic mechanisms through which these forebrain afferents act on PAG-USV neurons and PAG interneurons to exert their opposing effects on USV production. This study provides the first functional description of the synaptic logic that governs the decision to vocalize, a behavior fundamental to communication and survival.

Results

Inhibitory neurons in the hypothalamus and amygdala provide input to the PAG vocal gating circuit

To identify forebrain neurons that provide input to the PAG vocal gating circuit, we performed transsynaptic tracing from PAG-USV neurons, which are primarily glutamatergic and reside in the caudolateral PAG (Tschida et al., 2019). Briefly, to label inputs to PAG-USV neurons, we used an activity-dependent labeling strategy (CANE; see Methods) to express Cre-dependent helper viruses in PAG-USV neurons (Rodriguez et al., 2017; Sakurai et al., 2016; Tschida et al., 2019). A pseudotyped replication-deficient rabies virus was subsequently injected into the caudolateral PAG, allowing selective transsynaptic labeling of direct inputs to PAG-USV neurons (Fig. 1A, see Methods). Due to the difficulty in eliciting robust and reliable USVs from female mice, transsynaptic tracing from CANE-tagged PAG-USV neurons was performed only in male mice. Because the activity of many glutamatergic PAG neurons is shaped by potent inhibition from GABAergic PAG neurons (Tovote et al., 2016), we also performed transsynaptic tracing from local GABAergic neurons in the caudolateral and ventrolateral PAG that likely provide inhibition onto PAG-USV neurons, an idea we confirmed in a later section of the Results. To label direct inputs to local GABAergic PAG interneurons, Cre-dependent helper viruses were injected into the caudo/ventrolateral PAG of a VGAT-Cre mouse, and a pseudotyped replication-deficient rabies virus was subsequently injected at the same site to enable transsynaptic tracing from these cells (Fig. 1B; N=4 males, N=2 females). These rabies tracing experiments revealed monosynaptic inputs to PAG-USV neurons as well as to local GABAergic PAG neurons from a variety of forebrain areas (Table 1, Fig. S1-4). We subsequently focused on thoroughly characterizing forebrain afferents from the hypothalamus and amygdala, two brain regions important for the regulation and production of emotional and

social behaviors, including vocalization (Chen and Hong, 2018; Duvarci and Pare, 2014; Ehrlich et al., 2009; Gothard et al., 2020; Janak and Tye, 2015; LeDoux, 2007; Sternson et al., 2013).

Within the hypothalamus, we observed labeling of neurons in the medial preoptic area (POA, Fig. 1A-B), a region that plays a crucial role in sexual behavior (Balthazart and Ball, 2007; McKinsey et al., 2018; Newman, 1999; Wei et al., 2018) and more specifically in the production of courtship vocalizations in rodents and in songbirds (Alger and Riters, 2006; Bean et al., 1981; Floody, 1989, 2009; Floody et al., 1998; Fu and Brudzynski, 1994; Gao et al., 2019; Riters and Ball, 1999; Vandries et al., 2019). Within the amygdala, we observed inputs to both PAG cell types from neurons spanning the rostral portion of the boundary between the central and medial amygdala (referred to here as the central-medial boundary zone ($Amg_{C/M}$), see below) continuing caudally to the central amygdala (CeA) (Fig. 1A-B). Although the amygdala contributes to the sensory processing of and behavioral responses to social and emotional vocalizations (Fecteau et al., 2007; Gadziola et al., 2016; Hall et al., 2013; Schönfeld et al., 2020), whether and how the amygdala contributes to the *production* of vocalizations remains understudied (see Hall et al., 2013, Ma and Kanwal, 2014; Matsumoto et al., 2012).

To characterize the neurotransmitter phenotypes of these upstream hypothalamic and amygdala neurons, we performed two-color *in situ* hybridization on transsynaptically labeled neurons for mRNA transcripts expressed in glutamatergic and GABAergic cells (vesicular glutamate transporter (vGluT2) and vesicular GABA transporter (VGAT); Fig. 1C, see Methods). This experiment revealed that the majority (~84%, Fig. 1C-D) of PAG-projecting POA neurons (i.e. POA_{PAG} neurons) and almost all (~98%, Figure 1D) of PAG-projecting $Amg_{C/M}$ and CeA neurons (i.e. $Amg_{C/M\text{-}PAG}$ and CeA_{PAG} neurons) are GABAergic. In summary, the PAG vocal gating circuit receives input from inhibitory neurons in both the preoptic hypothalamus and the amygdala.

Activating PAG-projecting POA neurons elicits USVs in the absence of social cues

The POA plays a crucial role in courtship, raising the possibility that POA_{PAG} neurons are important to promoting USV production. To test this idea, we selectively expressed channelrhodopsin (ChR2) in POA_{PAG} neurons by injecting a Cre-dependent AAV driving ChR2 expression into the POA and injecting a retrogradely-infecting AAV that drives Cre expression into the caudolateral PAG, the region in which PAG-USV neurons are concentrated (Fig. 2A). Optogenetic activation of POA_{PAG} cell bodies was sufficient to elicit USVs in male and female mice that were singly tested in the absence of social partners or social cues (USVs elicited in N=6 of 8 males, N=3 of 4 females; 10 Hz trains or tonic pulses of 1-2s duration; Fig. 2A-B, Movie S1). Although optogenetic activation of POA_{PAG} neurons often elicited robust USV production, the efficacy of optogenetic stimulation (number of USVs elicited per trial, number of successful trials) as well as the latency from stimulation to USV onset were variable both within and across individual mice (Fig. 2B, F). This vocal effect was specifically attributable to optogenetic activation of the POA, as delivery of blue light to the POA of GFP-expressing mice failed to elicit USVs (AAV-FLEX-GFP injected into the POA of Esr1-Cre males, see below for additional Esr1-Cre data, N=5, Fig. 2F). In summary, optogenetic activation of POA_{PAG} neurons is capable of promoting USV production in both male and female mice, consistent with the known role of the POA in promoting appetitive courtship behaviors.

To begin to describe the molecular phenotype of POA_{PAG} neurons, we used situ hybridization to establish that these cells express VGAT (319/319 neurons were $VGAT^{+}$; Fig. 2C), similar to the POA neurons that we labeled via transsynaptic tracing from the PAG vocal gating circuit. We also noted that the majority of POA_{PAG} neurons co-express Estrogen Receptor 1 (Esr1), a prominent marker for neurons in the POA (278/319 Fig. 2C) (Fang et al., 2018; Moffitt et al., 2018; Wei et al., 2018). Given that POA_{PAG} neurons express Esr1, we next tested whether optogenetic activation of $Esr1^{+}$ POA neurons was sufficient to elicit USV production, by injecting a Cre-dependent AAV driving the expression of ChR2 into the POA of Esr1-Cre mice. We

observed that optogenetically activating Esr1$^+$ POA neurons was sufficient to elicit USV production in male (N=4 of 5) and female mice (N=3 of 4) that were tested in the absence of any social partners or social cues (Fig. 2D). In contrast, optogenetic activation of VGlut2$^+$ neurons within the POA failed to elicit USV production (Fig. 2F, N=3 males, POA of VGlut-Cre mice injected with AAV-FLEX-ChR2). Our findings confirm and extend the recent finding that optogenetic activation of GABAergic POA neurons elicits USV production in male and female mice (Gao et al., 2019).

To test whether activation of the Esr1$^+$ POA neurons that project to the PAG is sufficient to elicit USVs, we optogenetically activated the axon terminals of Esr1$^+$ POA neurons within the PAG (Fig. 2E). Bilateral Esr1$^+$ POA_{PAG} terminal activation within the PAG was sufficient to elicit USV production (N=1 of 2 males; N=4 of 6 females, 20 Hz trains of 2-10s duration). This treatment also evoked escape behavior in 4 of 8 of the tested animals, which was not observed following optogenetic activation of Esr1$^+$ POA cell bodies, suggesting that viral spread to PAG-projecting neurons nearby to the POA may account for these effects. Finally, we sought to test the idea that optogenetic activation of Esr1$^+$ POA neurons promotes USV production through their projections to the PAG rather than through other regions that they also innervate, and we also tested whether USV production could be elicited by activating non-POA hypothalamic inputs to the PAG. In fact, USVs were not elicited by optogenetically activating either Esr1$^+$ POA axon terminals in the ventral tegmental area (VTA) (Fig. 2F, 0/2 females, 0/2 males) or PAG-projecting neurons within the ventromedial hypothalamus (VMH) (Fig. 2F, 0/3 males, AAV-retro-Cre injected in the PAG, AAV-FLEX-ChR2 injected in the VMH). Therefore, GABAergic POA neurons, including Esr1$^+$ cells, act via their synapses in the caudolateral PAG to promote USV production.

Although these control experiments are consistent with the idea that POA_{PAG} and Esr1$^+$ POA neurons act directly on the vocal gating mechanism in the PAG, a remaining possibility is that

they promote USV production through hedonic reinforcement. To control for this possibility, we performed real-time place preference tests in which optogenetic stimulation of either POA_{PAG} or $Esr1^+$ POA neurons was applied when mice were in only one of two sides of the test chamber. We observed that optogenetic activation of POA_{PAG} neurons drove a slightly negative place preference on average (mean PP=0.39 +/- 0.07 for N=7 mice; Fig. S5A) and that optogenetic activation of $Esr1^+$ POA cell bodies did not positively reinforce place preference (mean PP=0.46 +/- 0.02 for N=5 mice). In contrast, optogenetic activation of $Esr1^+$ POA axon terminals within the VTA positively reinforced place preference (mean PP=0.59 +/- 0.06, N=4 mice, Fig. S5A). We also note that when using the same stimulation parameters that were sufficient to elicit USVs, optogenetic activation of either POA_{PAG} or $Esr1^+$ POA neurons did not drive mounting of other mice (N=7 POA_{PAG}-ChR2 mice tested; N=4 POA-Esr1-ChR2 mice tested) nor did it induce overt locomotion (Fig. S5B). These experiments indicate that activation of POA_{PAG} neurons can elicit USVs in a manner that does not depend on positive reinforcement and without recruiting other courtship behaviors.

Because the POA lies upstream of the PAG, we anticipated that optogenetic activation of the POA would elicit USV production at longer latencies than observed for optogenetic activation of PAG-USV neurons. Indeed, we found that the minimum and mean latencies to elicit USVs by optogenetic stimulation of POA neurons were 664.5 +/- 320.9 ms and 1782.6 +/- 407.6 ms respectively (Fig. S6, calculated from N=9 POA_{PAG}-ChR2 and N=7 POA-Esr1-ChR2 mice). These latencies are longer than those observed when optogenetically activating PAG-USV neurons (PAG-USV activation: min. latency from laser onset to first USV was 23.4 ± 8.6 ms, mean latency was 406.6 ± 0.5 ms) (Tschida et al., 2019)) but are comparable to the latencies from optogenetic activation of the hypothalamus to observed effects on behavior that have been reported in other studies (Lin et al., 2011; Wei et al., 2018). We also found that USV bouts elicited by optogenetic activation of the POA often outlasted the duration of the optogenetic

stimulation, sometimes by many seconds (Figs. 2, S6). This contrasts with what is observed following optogenetic activation of PAG-USV neurons, in which USV bout durations map on tightly to the duration of optogenetic stimulation (Tschida et al., 2019), and suggests that brief optogenetic stimulation in the POA can be transformed into longer-lasting changes in neural activity within the POA or across POA-to-PAG synapses.

Acoustic characterization of USVs elicited by activation of POA neurons

Given that optogenetic stimulation of the POA elicited USVs in the absence of any social cues, we wondered whether such optogenetically-evoked USVs were acoustically similar to the USVs that mice produce during social interactions. To compare the acoustic features of optogenetically-elicited USVs to those of USVs produced spontaneously to a nearby female, we employed a recently described method using variational autoencoders (VAEs) (Goffinet, 2019; Sainburg et al., 2019). Briefly, the VAE is an unsupervised modeling approach that uses spectrograms of vocalizations as inputs and from these data learns a pair of probabilistic maps, an “encoder” and a “decoder,” capable of compressing vocalizations into a small number of latent features while attempting to preserve as much information as possible (Fig. 3A-B). Notably, this method does not rely on user-defined acoustic features, nor does it require clustering of vocalizations into categories. We applied this approach to spectrograms of USVs to compare the acoustic features of female-directed and optogenetically-elicited USVs from the same mice and found that the VAE converged on a concise latent representation of only five dimensions. We then employed a dimensionality reduction method (UMAP) (McInnes, 2018) to visualize the latent features of these USVs in 2D space (Fig. 3C). This analysis revealed that for some mice, female-directed and optogenetically-elicited USVs were acoustically similar (Fig. 3C, left), while for other mice, a subset of optogenetically-elicited USVs were acoustically distinct from female-directed USVs (Fig. 3C, right). To quantify the difference between female-directed and optogenetically-elicited USVs for each mouse, we estimated the Maximum Mean

Discrepancy (Gretton, 2012) between distributions of latent syllable representations as in (Goffinet, 2019). In addition, a baseline level of variability in syllable repertoire was established for each mouse by estimating the MMD between the first and second halves of female-directed USVs emitted in a recording session (Fig. 3D). A paired comparison revealed significantly larger differences between female-directed and optogenetically-elicited USVs than expected by variability within the female-directed recording sessions alone (Fig. 3D, two-sided, continuity-corrected Wilcoxon signed-rank test, $W=5$, $p<0.01$), or than expected by across-day variability in female-directed recording sessions from control animals (gray points, Fig. 3D, female-directed USVs were recorded on 2 different days from $N=10$ control mice, $p=0.003$ for difference between female-directed vs. female-directed in control mice and opto vs. female-directed in experimental mice, Mann Whitney U test). In conclusion, many USVs elicited by optogenetic activation of POA neurons resemble female-directed USVs, although a subset differs in their acoustic features from USVs found in the animals' female-directed repertoires.

We next sought to understand in more detail exactly how these acoustically unusual optogenetically-elicited USVs differed from natural USVs. When the latent representations of these two types of USVs were plotted together for all mice in our dataset, it became clear that optogenetically-elicited USVs and female-directed USVs are largely acoustically overlapping except in one region of the UMAP representation (upper middle portion of Fig. 3E, dominated by blue points). Despite this outlying region of acoustically distinct optogenetically-elicited USVs, we conservatively estimate that only 20% of condition information (optogenetically-elicited versus female-directed) can be predicted by latent syllable descriptions, consistent with largely overlapping distributions of natural and optogenetically-elicited USVs (0.20 bits, 5-fold class-balanced logistic regression). We then re-plotted UMAP representations of the USVs, with each USV syllable color-coded according to syllable energy (i.e., amplitude, Fig. 3F, left) or frequency bandwidth (Fig. 3F, right). This analysis revealed that the acoustically unusual optogenetically-

elicited USVs tended to be louder and had greater frequency bandwidths than female-directed USVs. Visual inspection of spectrograms of optogenetically-elicited USVs also confirmed that those that did not overlap acoustically with natural USVs tended to be louder and have greater frequency bandwidths (Fig. 3F, bottom, opto 1 and opto 2), while optogenetically-elicited USVs that overlapped with natural USVs did not possess these unusual acoustic features (Fig. 3F, bottom, opto 3). To determine whether the differences between optogenetically-elicited and natural USVs were consistent across mice, we summarized each recording session by the mean latent representation of its syllables, and then summarized the shift from natural to optogenetically-elicited syllable repertoires by the corresponding vector between summary points. A shuffle test revealed significantly larger alignment between these vectors than expected by chance (mean cosine similarity=0.50, $p<1e-5$), indicating that optogenetically-elicited USVs differed from female-directed USVs in a manner that was consistent across mice. In summary, optogenetic activation of the POA elicits USVs whose acoustic features are largely overlapping with those of female-directed USVs produced by the same animal, despite the artificiality inherent to optogenetic stimulation.

Activating PAG-projecting $Amg_{C/M}$ neurons transiently suppresses USV production

We next sought to understand how PAG-projecting amygdala neurons contribute to vocalization. We began with a viral strategy designed to express ChR2 in PAG-projecting $Amg_{C/M}$ and CeA neurons, by injecting a Cre-dependent AAV driving ChR2 expression targeted to the amygdala and then injecting AAV-retro-Cre into the PAG (Fig. 4). Surprisingly, given the strong transsynaptic labeling of both the CeA and $Amg_{C/M}$ achieved with modified rabies tracing from the PAG vocal gating circuit, we found that this viral strategy failed to label neurons in the CeA and instead only labeled $Amg_{C/M}$ neurons, whose cell bodies reside medial to the CeA and dorsal to the medial amygdala (Figs. 4A, S7). To ensure that this labeling pattern was due to restricted tropism of the AAV-retro-Cre virus and not to inaccurate targeting of the CeA, we

repeated the injections of the AAV-retro-Cre virus in the PAG of a Cre-dependent tdTomato reporter mouse. Again, we observed cell body labeling in the $Amg_{C/M}$ but not in the CeA (Fig. S8), suggesting that in contrast to the modified rabies virus used in the transsynaptic tracing from the PAG vocal gating circuit, the AAV-retro-Cre virus can infect $Amg_{C/M}$ but not CeA neurons.

To test whether PAG-projecting $Amg_{C/M}$ neurons influence USV production, we first tested the effects of optogenetically activating these neurons in isolated mice. Optogenetic activation of $Amg_{C/M\text{-}PAG}$ neurons failed to elicit USV production and also did not drive any other overt behavioral effects. However, when $Amg_{C/M\text{-}PAG}$ neurons were optogenetically activated in male mice that were actively courting females and vocalizing, USV production was immediately and reversibly suppressed (Fig. 4B, N=8 mice). This suppressive effect was restricted to the period when $Amg_{C/M\text{-}PAG}$ neurons were being optogenetically stimulated, and USV production rebounded following the end of the optogenetic stimulation period (Fig. 4B). After using *in situ* hybridization to confirm that most $Amg_{C/M\text{-}PAG}$ neurons are GABAergic (~92% $Amg_{C/M\text{-}PAG}$ neurons express VGAT, Fig. 4C), we used a similar intersectional viral strategy to express ChR2 selectively in GABAergic $Amg_{C/M\text{-}PAG}$ neurons (Fig.4D, AAV-retro-FLEX-ChR2 injected into the PAG of a VGAT-Cre mouse). With this strategy, we found that optogenetic activation of GABAergic $Amg_{C/M\text{-}PAG}$ neurons robustly suppressed the male's USV production during courtship encounters with a female (Fig. 4D, N=4 male mice). Finally, we tested the effects on vocal behavior of optogenetically activating the axon terminals of GABAergic $Amg_{C/M\text{-}PAG}$ neurons within the PAG (Fig. 4D). Such bilateral terminal activation was also sufficient to suppress USV production (in N=3 of 3 males; Fig. 4D).

One possibility is that activating $Amg_{C/M\text{-}PAG}$ neurons suppresses USV production by putting the mouse into a fearful or aversive state, rather than through a direct suppressive effect of $Amg_{C/M\text{-}PAG}$ neurons on the PAG vocal gating circuit. To test this idea, we carefully examined the non-

vocal behaviors of male mice during optogenetic activation of $Amg_{C/M-PAG}$ neurons. Mice exhibited neither freezing nor fleeing during optogenetic stimulation of $Amg_{C/M-PAG}$ neurons and, more notably, they usually continued to follow and sniff the female during the laser stimulation periods (Movie S2; distance between male and female did not increase during optogenetic stimulation, Fig. S5B). We also confirmed that the change in USV production rates driven by the optogenetic activation of $Amg_{C/M-PAG}$ neurons was different from the change in spontaneous USV rates over time in mice that did not receive laser stimulation (Fig. 4D, black trace), the change in USV rates over time in GFP control mice (Fig. 4D, green trace), and the change in USV rates over time in $Amg_{C/M-PAG}$-ChR2-expressing mice that were connected to a dummy ferrule that only shined blue light over their head (Fig. 4D, gray trace; $p<0.01$ for differences between ChR2 groups vs. control groups during laser time, one-way ANOVA followed by post-hoc pairwise Tukey's HSD tests). Finally, we performed real-time place preference tests in which $Amg_{C/M-PAG}$ neurons were optogenetically activated when mice were in one of two sides of a test chamber ($Amg_{C/M-PAG}$ neurons were labeled with either the AAV-retro-Cre or the AAV-retro-ChR2 viral strategies). This experiment revealed that activation of $Amg_{C/M-PAG}$ neurons does not drive a negative place preference (Fig. S5A). In summary, activating $Amg_{C/M-PAG}$ neurons transiently and selectively suppresses USVs produced by male mice during courtship, an effect that cannot be accounted for by the mouse being put into a fearful or aversive state.

Axonal projections of POA_{PAG} and $Amg_{C/M-PAG}$ neurons

To further characterize the anatomy of POA_{PAG} and $Amg_{C/M-PAG}$ neurons, we used intersectional methods to label these neurons with GFP and tdTomato respectively and traced their axonal projections throughout the brain (Fig. S9, AAV-retro-Cre injected into caudolateral PAG, AAV-FLEX-GFP into POA, AAV-FLEX-tdTomato into $Amg_{C/M}$). We observed dense projections from both POA_{PAG} and $Amg_{C/M-PAG}$ neurons to a variety of dopaminergic cell groups, including the VTA, SNc and retrorubral/A8 region. We also note that $Amg_{C/M-PAG}$ neurons provide input to the

lateral preoptic area (Fig. S9, top left), while POA_{PAG} neurons provide input to the same region in which $Amg_{C/M-PAG}$ cell bodies reside (Fig. S9, middle left). As expected, we also observed dense and overlapping terminal fields from both of the cell groups within the caudolateral PAG (Fig. S9, bottom right).

Synaptic interactions between POA_{PAG} and $Amg_{C/M-PAG}$ neurons and the PAG vocal gating circuit

The functional and anatomical experiments described above establish that two different populations of inhibitory forebrain neurons provide input to the PAG vocal gating circuit, one of which (the POA) promotes USV production in the absence of any social cues, while the other (the $Amg_{C/M}$) suppresses spontaneous USVs produced by male mice during courtship. To understand how two different GABAergic and presumably inhibitory inputs to the PAG can exert opposing effects on vocal behavior, we performed ChR2-assisted circuit mapping experiments in brain slices to characterize the properties of POA and $Amg_{C/M}$ synapses onto PAG-USV neurons and nearby GABAergic PAG neurons.

Given that optogenetic activation of GABAergic $Amg_{C/M-PAG}$ neurons suppresses USV production, we predicted that GABAergic $Amg_{C/M}$ neurons directly inhibit PAG-USV neurons. To test this idea, we performed whole-cell voltage clamp recordings from PAG-USV neurons while optogenetically activating $Amg_{C/M-PAG}$ axons within the PAG. Briefly, AAV-FLEX-ChR2 was injected into the $Amg_{C/M}$ of a VGAT-Cre;Fos-dsTVA crossed mouse in order to express ChR2 in GABAergic $Amg_{C/M-PAG}$ axon terminals within the PAG. After four weeks, we used the CANE method (Rodriguez et al., 2017; Sakurai et al., 2016; Tschida et al., 2019) to infect PAG-USV neurons with a pseudotyped CANE-rabies virus driving the expression of mCherry (CANE-RV-mCherry, Fig. 5A-B, see Methods). We visually targeted our recordings to mCherry-expressing PAG-USV neurons and optogenetically activated $Amg_{C/M}$ terminals in the presence of TTX and 4AP in order to isolate monosynaptic pathways (Fig. 5C-D). Activating $Amg_{C/M-PAG}$ terminals

evoked inhibitory postsynaptic currents (IPSCs) in a majority (16/29) of the mCherry-labeled PAG-USV neurons from which we recorded (mean current=180.3 pA at 0 mV in TTX/4AP). These evoked IPSCs were completely abolished by application of the $GABA_A$ receptor antagonist gabazine (Fig. 5E-F). No optogenetically-elicited EPSCs were detected when recording at -70 mV, the chloride reversal potential. These findings support the idea that $Amg_{C/M\text{-}PAG}$ activity suppresses ongoing USV production by directly inhibiting PAG-USV neurons.

Given that activating GABAergic POA_{PAG} neurons elicits vocalization (Fig. 2), and that the majority of PAG-USV neurons are glutamatergic (Tschida et al., 2019), we hypothesized that POA_{PAG} axons act via local GABAergic interneurons in the PAG to disinhibit PAG-USV neurons. To test this hypothesis, we first performed whole-cell patch clamp recordings from GABAergic PAG neurons while optogenetically activating POA_{PAG} axons within the PAG. GABAergic PAG neurons were labeled by injecting AAV-FLEX-mCherry into the PAG of a VGAT-Cre mouse, while AAV-FLEXa-ChR2 was injected into the POA to express ChR2 in POA_{PAG} axon terminals within the PAG (Fig. 6A-B). After waiting four weeks to achieve functional expression of ChR2 in POA_{PAG} axon terminals, we cut brain slices from these mice and recorded optogenetically-evoked currents from fluorescently identified $VGAT^+$ PAG neurons (see Methods). Optical stimulation of POA_{PAG} axons with blue light evoked IPSCs in the majority (26/36) of voltage clamped GABAergic PAG neurons from which we recorded (mean current=328.8 pA at 0 mV) (Fig. 6C). These evoked IPSCs persisted upon application of TTX/4AP and were blocked by gabazine, indicating that POA_{PAG} axons make inhibitory synapses directly onto GABAergic PAG neurons (Fig. 6D).

To test whether these GABAergic PAG neurons synapse onto PAG-USV neurons, as predicted of a disinhibitory circuit mechanism, we injected AAV-FLEX-ChR2 into the PAG of a VGAT-Cre;TVA crossed mouse in order to express ChR2 in local $VGAT^+$ neurons (Fig. 6E). After two

weeks, we used CANE to selectively infect PAG-USV neurons with CANE-RV-mCherry (Fig. 6). Several days later, we visually targeted mCherry-expressing PAG-USV neurons for whole-cell recordings while optogenetically activating local GABAergic PAG neurons in the presence of TTX and 4AP (Fig. 6F). Optogenetically activating local VGAT^{+} neurons evoked IPSCs in almost all (13/16) of the PAG-USV neurons from which we recorded (mean current=579.9 pA at 0 mV in TTX/4AP) and these currents were completely abolished by application of gabazine (Fig. 6G-H). This experiment confirms the presence of a functional connection between local inhibitory neurons and the PAG-USV neurons that gate USV production.

We also performed whole-cell recordings from mCherry-labeled PAG-USV neurons while optogenetically activating POA_{PAG} axons within the PAG (AAV-FLEX-ChR2 injected into the POA of a VGAT-Cre;Fos-dsTVA crossed mouse, CANE method used to infect PAG-USV neurons with CANE-RV-mCherry as described above; Fig. S10A, see Methods). After first confirming that we could optogenetically evoke IPSCs in mCherry-negative cells in each slice, we visually targeted our recordings to mCherry-expressing PAG-USV neurons. Optogenetic activation of POA_{PAG} terminals evoked IPSCs in only 1 of 23 PAG-USV neurons (Fig. S10B). Although there are caveats to interpreting a low probability of synaptic connection in brain slices, POA_{PAG} neurons appear to provide fewer or weaker synaptic inputs to PAG-USV neurons than to nearby GABAergic PAG neurons, supporting the idea that POA_{PAG} neurons primarily act through PAG interneurons to disinhibit PAG-USV neurons and promote USV production.

Discussion

Here we used a combination of monosynaptic rabies tracing, optogenetic manipulations of neural activity in freely behaving animals, and optogenetics-assisted circuit mapping in brain slices to elucidate the functional relevance and synaptic organization of descending inputs to

the PAG vocal gating circuit. We identified two populations of forebrain inhibitory neurons, one located in the preoptic hypothalamus and the other in a central-medial boundary zone within the amygdala, that drive opposing effects on vocal behavior. Optogenetic activation of POA_{PAG} neurons drives robust and long-lasting bouts of vocalization in the absence of any social cues normally required to elicit vocalizations, and the acoustic features of optogenetically-elicited USVs shared many features with spontaneously produced social USVs. In contrast, optogenetic activation of a $VGAT^{+}$ population of $Amg_{C/M\text{-}PAG}$ neurons transiently suppressed USV production in male mice during active courtship without disrupting other non-vocal courtship behaviors. Further, activation of $Amg_{C/M\text{-}PAG}$ neurons did not elicit fearful or aversive behavior, indicating that the effect on vocal behavior was not driven or accompanied by a generalized change in behavioral state. Finally, we paired optogenetic activation of descending POA or $Amg_{C/M}$ inputs to the PAG with whole-cell recordings from PAG-USV or GABAergic PAG neurons to investigate how these POA and $Amg_{C/M}$ inputs drive opposing effects on vocal behavior. These slice experiments support a model in which $Amg_{C/M\text{-}PAG}$ neurons directly inhibit PAG-USV neurons to suppress vocalization, while POA_{PAG} neurons directly inhibit GABAergic PAG interneurons, which in turn inhibit PAG-USV neurons, resulting in a net disinhibition of PAG-USV neurons that promotes vocalization. To our knowledge, this is the first study to reveal the synaptic and circuit logic by which forebrain afferents to the PAG influence the decision to vocalize, a key behavior for communication and survival.

We observed that, when optogenetically activated, POA_{PAG} neurons act directly through the PAG to elicit USV production in both male and female mice (Fig. 2), confirming and extending a recent report that activation of GABAergic POA neurons elicits USVs in both sexes (Gao et al., 2019). These findings contrast with the behavioral observation that female mice in general produce fewer USVs than males. For example, female mice produce only about 1/5 of the total USVs recorded during male-female courtship interactions (Neunuebel et al., 2015), and we

observed that female mice vocalize at lower rates than males when encountering novel female social partners (unpublished observations). Taken together, these findings suggest that different levels of POA_{PAG} activity in males and females might contribute to sex differences in vocal behavior but, when strongly activated by optogenetic methods, POA_{PAG} neurons in males and females are similarly potent in their ability to activate the downstream PAG vocal gating circuit and elicit USVs. Although it remains unknown which factors might drive differential activation of male and female POA_{PAG} neurons, it is possible that sex differences in the density (Campi et al., 2013; Gorski et al., 1978; Orikasa and Sakuma, 2010; Panzica et al., 1996), synaptic organization (Raisman and Field, 1971), and gene expression patterns (Moffitt et al., 2018; Xu et al., 2012), including those of sex hormone receptors (Cao and Patisaul, 2013) of POA neurons, might all contribute to this sexually dimorphic behavior (for a review, see Lenz et al., 2012). More broadly, our findings add to a growing body of literature indicating that male and female brains contain latent circuits for sex-typical behaviors that can be unmasked by artificial neural activation but that are gated in a sex-specific manner during natural behavior (Clyne and Miesenbock, 2008; Gao et al., 2019; Rezaval et al., 2016; Wei et al., 2018).

We also found that similar to activation of POA_{PAG} neurons, optogenetic activation of $Esr1^+$ POA neurons was sufficient to elicit USV production. Although a previous study reported that activation of $Esr1^+$ POA neurons promotes mounting (Wei et al., 2018), we failed to observe mounting when we optogenetically activated either POA_{PAG} neurons or $Esr1^+$ POA neurons in male and female mice. Although the reasons for this discrepancy remain uncertain, one possibility is that our use of lower intensity optical stimulation can account for this difference (3-5 mW, 10-20 Hz vs. 10mW, 40 Hz in Wei et al., 2018), and that the level of $Esr1^+$ POA neuronal activation required to elicit USV production is lower than the threshold to elicit mounting. An interesting possibility is that different projection-defined subsets of $Esr1^+$ POA neurons contribute to distinct aspects of courtship behavior, similar to what has been described for the

contribution of projection-defined subsets of galanin-expressing POA neurons to distinct aspects of parental behavior (Kohl et al., 2018; Wu et al., 2014). Notably, though, a recent study found that ablation of VGAT^{+} POA neurons did not affect the numbers of social USVs produced by male and female mice, although the acoustic features of male courtship USVs were altered following ablation of these neurons (Gao et al., 2019). In contrast, ablation or silencing of POA neurons greatly reduces non-vocal consummatory courtship behaviors including mounting and ejaculation (Bean et al., 1981; Floody, 1989; Wei et al., 2018). These findings are consistent with the idea that POA_{PAG} neurons promote the production of USVs during later stages of courtship (Gao et al., 2019), which differ acoustically from USVs produced in earlier phases of courtship (Hanson and Hurley, 2012; Keesom et al., 2017; Matsumoto and Okanoya, 2016; White et al., 1998). These findings also suggest that other neuronal populations that lie upstream of the PAG vocal gating circuit, and that are potentially interconnected with the POA, serve to promote USV production during the early phases of courtship and in other behavioral contexts.

Here we employ a newly described VAE-based unsupervised modeling method to compare the acoustic features of optogenetically-elicited USVs to each animal's repertoire of female-directed USVs. Interestingly, although synchronous optogenetic activation of POA_{PAG} neurons is likely quite different from the natural activity patterns of these neurons, the majority of optogenetically-elicited vocalizations fall within the distribution of naturally produced USVs. This finding provides further experimental support for a model in which the PAG-USV neurons that are disinhibited by input from the POA gate USV production but do not directly pattern the acoustic content of vocalizations. The VAE also allowed us to identify and interrogate the acoustic features of optogenetically-elicited vocalizations that fell outside the natural acoustic distribution. We found that these unusual optogenetically-elicited USVs were louder and greater in frequency bandwidth, which we speculate may arise because synchronous optogenetic activation of POA

neurons activates the PAG vocal gating circuit more strongly than occurs during natural behavior. Another possibility is that because the mice in our experiments were singly tested in the absence of social partners and thus typically were not moving at high speeds during optogenetic stimulation, the USVs elicited by optogenetic stimulation of POA_{PAG} neurons may be more similar acoustically to spontaneous USVs emitted in response to stationary social cues, such as female urine, rather than in response to a mobile female partner. Interestingly, a previous study found that the USVs produced by males in response to female urine were louder and had greater frequency bandwidth than those produced to female social partners (Chabout et al., 2015), reminiscent of the difference between female-directed and optogenetically-evoked USVs in our dataset.

The current study also identifies a novel population of GABAergic $Amg_{C/M\text{-}PAG}$ neurons that lie at a boundary zone between the central amygdala and the medial amygdala and that project to PAG-USV neurons (i.e., $Amg_{C/M\text{-}PAG}$ neurons). Although this population of cells remains to be characterized comprehensively at a molecular and physiological level, our data show that transiently activating these neurons transiently suppresses USV production without driving fearful or aversive responses. Additionally, optogenetically activating $Amg_{C/M\text{-}PAG}$ neurons suppresses vocalization without interrupting non-vocal courtship behaviors more generally, providing additional support for the idea that PAG-USV cells are specialized neurons that gate USV production but that do not control non-vocal aspects of courtship.

We found that $Amg_{C/M\text{-}PAG}$ neurons make inhibitory synapses on PAG-USV neurons, which in turn gate vocalizations by exciting downstream vocal-respiratory pattern generating circuits (Tschida et al., 2019). Thus, the $Amg_{C/M}$ to PAG pathway provides a monosynaptic substrate through which vocalizations can be rapidly and effectively suppressed. We anticipate that such descending inhibitory inputs onto PAG-USV neurons act rapidly to suppress vocalization in behavioral contexts (in the presence of predators, conspecific competitors, etc.) in which

vocalizing is risky or otherwise adverse, although this idea remains to be tested. Although POA_{PAG} neurons are also GABAergic, we found that optogenetically activating these neurons promotes rather than suppresses USV production, likely through a disynaptic disinhibition of PAG-USV neurons mediated by local PAG interneurons. Consistent with the idea that disinhibition within the PAG is important for vocal production, work in primates has shown that pharmacological blockade of GABA receptors lowers the threshold for vocalization and elicits spontaneous vocalizations as well (Forcelli et al., 2017; Jurgens, 1994; Lu and Jurgens, 1993). Indeed, disinhibition of glutamatergic projection neurons has emerged as a prominent circuit motif within the PAG for releasing a variety of behaviors, including freezing (Tovote et al., 2016), pup grooming (Kohl et al., 2018), and antinociception (Morgan and Clayton, 2005). Our results support a model in which PAG-USV neuronal activity is tightly regulated by descending inputs as well as inputs from local GABAergic PAG neurons, which in turn integrate a variety of behaviorally relevant forebrain inputs to appropriately gate PAG-USV activity and hence USV production. More generally, such disinhibitory circuit motifs in the PAG may provide a failsafe mechanism that carefully regulates the behavioral contexts in which crucial but potentially costly behaviors, including vocalization, are produced.

By exploiting selective genetic access to PAG-USV neurons as a point of entry into central circuits for social and courtship vocalizations, we have begun to map the brain-wide architecture and synaptic organization of circuitry for a complex, natural behavior. In addition to the inputs from the POA and $Amg_{C/M}$ that were the focus of this study, our transsynaptic tracing identified a number of forebrain regions whose projections converge onto the PAG vocal gating circuit, consistent with the idea that the PAG integrates a wide variety of social, environmental, and interoceptive information to gate vocalization in a context-appropriate manner. Given that context-dependent vocal gating is a hallmark of human vocalizations, including speech (Stivers et al., 2009), it will be of great interest in future studies to more fully describe the neuronal

populations whose inputs to the PAG shape vocal behavior. We note that vocal behavior is not simply binary: in addition to deciding whether or not to vocalize, an animal must produce vocalizations that are appropriate for a given situation. The elucidation of circuit and synaptic mechanisms through which forebrain inputs to the PAG vocal gating circuit influence USV production represents an important first step toward understanding how forebrain-to-midbrain circuits regulate the production of vocalizations across different behavioral contexts to enable effective communication.

Materials and Methods

CONTACT FOR REAGENT AND RESOURCE SHARING

Further information and requests for resources and reagents should be directed to the co-corresponding authors, Katherine Tschida (kat227@cornell.edu) or Richard Mooney (mooney@neuro.duke.edu).

EXPERIMENTAL MODELS AND SUBJECT DETAILS

Animal statement. All experiments were conducted according to protocols approved by the Duke University Institutional Animal Care and Use Committee.

Animals. For optogenetic activation and axonal tracing experiments, the following mouse lines from Jackson labs were used: C57 (000664), Esr1-Cre (017911), VGAT-Cre (016962), Ai14 (007908). Fos-dsTVA mice (Jackson Labs, 027831) were used for activity-dependent labeling of PAG-USV neurons employed in the transsynaptic tracing experiments and in whole-cell recording experiments. In a subset of whole-cell recording experiments, VGAT-Cre homozygous mice were crossed to Fos-dsTVA homozygous mice.

METHOD DETAILS

Viruses: The following viruses and injection volumes were used: AAV2/1-hSyn-FLEX-ChR2-eYFP (Addgene), AAV-pgk-retro-Cre (Addgene), AAV-hsyn-retro-FLEX-ChR2 (Addgene), AAV-FLEX-GFP (Addgene), AAV-FLEX-tdTomato (Addgene), AAV-FLEX-oG (Duke Viral Vector Core). EnvA-ΔG-RV-GFP, CANE-RV-mCherry, and AAV-FLEX-TVA-mCherry were produced in house as previously described (Rodriguez et al., 2017; Sakurai et al., 2016; Tschida et al., 2019). The final injection coordinates were as follows: POA, AP=0.14 mm, ML= 0.3 mm, DV= 5.5 mm; $Amg_{C/M}$, AP=-1.5 mm, ML= 2.3 mm, DV= 4.6 mm; PAG, AP=-4.7 mm, ML= 0.7 mm,

DV= 1.75 mm. Viruses were pressure-injected with a Nanoject II (Drummond) at a rate of 4.6 nL every 15s.

Transsynaptic tracing from PAG-USV and GABAergic PAG neurons: To selectively infect PAG-USV neurons with viruses, ds-Fos-TVA males were given social experience with a female (30-60 mins.) that resulted in high levels of USV production (500-5000 USVs total). Males were then anesthetized (1.5-2% isoflurane), and the caudolateral PAG was targeted for viral injection. For transsynaptic tracing from PAG-USV neurons, the PAG was injected with a 4:1:1 mixture of CANE-LV-Cre, AAV-FLEX-TVA-mCherry, and AAV-FLEX-oG (total volume of 300 nL). After a wait time of 10-14 days, the PAG was then injected with EnvA-ΔG-RV-GFP (100 nL, diluted 1:5), and animals were sacrificed after waiting an additional 4-7 days.

To transsynaptically label inputs to GABAergic PAG neurons, the caudolateral PAG of VGAT-Cre mice was injected with a 1:1 mixture of AAV-FLEX-TVA-mCherry, and AAV-FLEX-oG (total volume of 100 nL). After a wait time of 10-14 days, the PAG was then injected with EnvA-ΔG-RV-GFP (100 nL, diluted 1:5), and animals were sacrificed after waiting an additional 4-7 days.

We note that because our goal was to identify long-range inputs onto PAG-USV and GABAergic PAG neurons, we used survival times that prioritized visualization of afferent cell bodies in distant locations rather than the integrity of the starter cell populations (which die off over time). Hence, we do not include quantification of starter cell populations within the PAG, as these cannot be meaningfully related to the numbers of cells that provide monosynaptic input to PAG-USV and GABAergic PAG neurons.

In vivo optogenetic stimulation: Custom-made or commercially available (RWD) optogenetic ferrules were implanted in the same surgeries as viral injection just above target brain locations and were fixed to the skull using Metabond (Parkell). Neurons or their axon terminals were optogenetically activated with illumination from a 473 nm laser (3-15 mW) at 10-20 Hz (50 ms

pulses, 2-10s total) or with phasic laser pulses (1-2s duration). Laser stimuli were driven by computer-controlled voltage pulses (Spike 7, CED).

Post-hoc visualization of viral labeling: Mice were deeply anaesthetized with isoflurane and then transcardially perfused with ice-cold 4% paraformaldehyde in 0.1 M phosphate buffer, pH 7.4 (4% PFA). Dissected brain samples were post-fixed overnight in 4% PFA at 4 °C, cryoprotected in a 30% sucrose solution in PBS at 4 °C for 48 hours, frozen in Tissue-Tek O.C.T. Compound (Sakura), and stored at –80 °C until sectioning. To visualize viral labeling post-hoc, brains were cut into 80 µm coronal sections, rinsed 3x in PBS, and processed for 24 hours at 4 degrees with NeuroTrace (1:500 Invitrogen) in PBS containing 0.3% Triton-X. Tissue sections rinsed again 3 x 10 mins. in PBS, mounted on slides, and coverslipped with Fluoromount-G (Southern Biotech). After drying, slides were imaged with a 10x objective on a Zeiss 700 laser scanning confocal microscope.

Floating section two-color *in situ* hybridization: *In situ* hybridization was performed using hybridization chain reaction (HCR v3.0, Molecular Instruments). Dissected brain samples were post-fixed overnight in 4% PFA at 4 °C, cryoprotected in a 30% sucrose solution in RNAse-free PBS (i.e., DEPC-PBS) at 4 °C for 48 hours, frozen in Tissue-Tek O.C.T. Compound (Sakura), and stored at –80 °C until sectioning. 80-µm thick coronal floating sections were collected into a sterile 24 well plate in DEPC-PBS, fixed again briefly for 5 min. in 4% PFA, then placed in 70% EtOH in DEPC-PBS overnight. Sections were rinsed in DEPC-PBS, incubated for 45 min in 5% SDS in DEPC-PBS, rinsed and incubated in 2x SSCT, pre-incubated in HCR hybridization buffer at 37 °C, and then placed in HCR hybridization buffer containing RNA probes overnight at 37 °C. The next day, sections were rinsed 4 x 15 minutes at 37 °C in HCR probe wash buffer, rinsed with 2X SSCT, pre-incubated with HCR amplification buffer, then incubated in HCR amplification buffer containing HCR amplifiers at room temperature for ~48 hours. On the final day, sections were rinsed in 2x SSCT, counterstained with DAPI (Thermo Fisher, 1:5000),

rinsed again with 2x SSCT, then mounted on slides and coverslipped with Fluoromount-G (Southern Biotech). After drying, slides were imaged with a 10x or 20x objective on a Zeiss 700 laser scanning confocal microscope. Cells were scored from 2-7 sections of tissue per brain region from each animal, and the absence or presence of staining within cells was quantified manually by comparing labeling within cells to background labeling in nearby regions known to be negative for a given RNA transcript.

USV recording and analysis. To elicit USVs, single-housed males or females were presented with a freely moving female, either in a novel test chamber or in the home cage. USVs were recorded with an ultrasonic microphone (Avisoft, CMPA/CM16), amplified (Presonus TubePreV2), and digitized at 250 kHz (Spike 7, CED). USVs were detected using codes from the Holy lab (http://holylab.wustl.edu/) using the following parameters (mean frequency > 45 kHz; spectral purity > 0.3; spectral discontinuity < 0.85; min. USV duration = 5 ms; minimum inter-syllable interval = 30 ms). To elicit USVs for tagging of PAG-USV neurons using CANE (for transsynaptic tracing and slice experiments), Fos^{TVA} males were given social experience with a female (30-60 min. session), either in their home cage fitted with an acoustically permeable lid or in a test chamber that had no lid and allowed easy microphone access. Sixty minutes from the start of the session, Fos^{TVA} males were anesthetized and taken for injection of the PAG with viruses (see above), such that injections began approximately 2 hours from the start of USV production.

Real-time place preference tests: Mice were lightly anesthetized to connect the 473 nm laser to the optogenetic ferrule, then mice were placed in the center of a custom-made two-sided test chamber, illuminated with infrared light only. The side of the chamber in which each mouse received optogenetic stimulation was chosen randomly for each place preference test. When the mouse was in the selected side, it received continuous 10 Hz optogenetic stimulation using the minimum laser power that had either elicited or inhibited USV production for that same

mouse. Place preference was scored over a 20 minute test period as the proportion of the total time that the mouse spent in the stimulated side of the chamber.

Quantification of optogenetically-elicited body movements: The mouse's position was measured using custom Matlab codes that detected and tracked the centroid of the mouse's body position across video frames (Logitech webcam, 30 frames per second), and speed of movement was calculated as the change in position across pairs of frames. To align movement with optogenetic activation of POA or $Amg_{C/M}$ neurons, we first estimated the temporal offset between the webcam video and USV audio by calculating the time of the peak cross-covariance between the high-pass filtered webcam audio and the low-pass filtered USV audio. This offset was then used to align the mouse's movement to the onset of each optogenetic laser stimulus. To measure the effects of optogenetic stimulation on the distance between an interacting male and female mouse, the position of each mouse was tracked manually in every 6th frame, and the distance between mice was scored as the distance from the center of the male's head to the base of the female's tail.

Comparison of acoustic features of optogenetically-elicited USVs to female-directed USVs: 52,821 USV syllables were segmented automatically with MUPET 2.0 using default parameter settings (Van Segbroeck et al., 2017). 23,805 of these syllables came from recordings of 15 mice recorded under both natural and optogenetic conditions (56% natural USVs). The remaining 29,016 syllables came from recordings of a control group of 10 mice used to establish across-day syllable repertoire variability. False positives (noise) from the experimental group were manually removed by visual inspection of spectrograms, with 79% of the original syllables retained. Syllables were analyzed using Autoencoded Vocal Analysis v0.2 (Goffinet, 2019), a Python package for generating low-dimensional latent descriptions of animal vocalizations using a variational autoencoder (VAE) (Kingma, 2013). Briefly, the VAE jointly trains two probabilistic maps: an encoder and a decoder. Spectrograms are encoded into low-

dimensional "latent" representations which can be subsequently decoded to approximately reconstruct the original spectrograms. Both encoding and decoding distributions are parameterized by convolutional neural networks. We trained a VAE on spectrograms of single USV syllables from both experimental and control groups using the following parameters: min_freq=30e3, max_freq=110e3, nperseg=1024, noverlap=512, spec_min_val=-5.0, spec_max_val=-1.5, mel=False, time_stretch=True, within_syll_normalize=False. Each input spectrogram was 128-by-128 pixels (16000 dimensions) and the VAE converged on a parsimonious representation of only 5 dimensions. To visualize these 5-dimensional spaces, the latent representations of syllable spectrograms are projected into two dimensions using the UMAP algorithm (McInnes, 2018). To quantify differences in syllable repertoires, we estimate the Maximum Mean Discrepancy (Gretton, 2012) between distributions of latent syllable representations as in (Goffinet, 2019). First, a baseline level of variability in syllable repertoire was established for each mouse by estimating MMD between the first and second halves of female-directed syllables emitted in a recording session. Then MMD between each mouse's natural and optogenetically-elicited repertoires was estimated. A paired comparison test revealed significantly larger differences between optogenetic and natural repertoires than expected by variability within the natural condition recording sessions alone (two-sided, continuity-corrected Wilcoxon signed-rank test, $W=9$, $p<5e-3$). We then estimated MMD between female-directed syllable repertoires recorded on different days, using the set of 10 control mice.

Whole-cell recordings: Mice that received viral injections 2-4 weeks prior were deeply anesthetized with isoflurane and standard procedures were used to prepare 300 µm thick coronal slices. The brain was dissected in ice-cold ACSF containing the following (in mM): 119 NaCl, 2.5 KCl, 1.30 $MgCl_2$, 2.5 $CaCl_2$, 26.2 $NaHCO_3$, 1.0 $NaHPO_4$-H_2O, and 11.0 dextrose and bubbled with 95% O_2/5% CO_2. The brain was mounted on an agar block and sliced in ice-cold

ACSF with a vibrating-blade microtome (Leica). Slices were incubated for 15 minutes at 32ºC in a bath of NMDG recovery solution containing the following (in mM): 93.0 NMDG, 2.5 KCl, 1.2 NaH_2PO_4, 30.0 $NaHCO_3$, 20.0 HEPES, 25.0 glucose, 2.0 thiourea, 5.0 Na L-ascorbate, 2.0 Na-pyruvate, 10.0 $MgSO_4$ $7H_2O$, 0.5 $CaCl_2$, and 95.0 HCl. Slices were then moved to a bath of HEPES storage solution containing the following (in mM): 93.0 NaCl, 2.5 KCl, 1.2 NaH_2PO_4, 30.0 $NaHCO_3$, 20.0 HEPES, 25.0 glucose, 2.0 thiourea, 5.0 Na L-ascorbate, 2.0 Na-pyruvate, 10.0 $MgSO_4$ $7H_2O$, and 0.5 $CaCl_2$, and allowed to gradually reach room temperature over the course of 1 hour, where they remained for the duration. Recordings were performed in ACSF at a temperature of 32ºC. For voltage clamp experiments patch electrodes (4-8 MΩ) were filled with cesium internal solution containing the following (in mM): 130 cesium methanesulfonate, 5 QX-314 Br, 10 HEPES, 8 TEA-Cl, 0.2 EGTA, 4 ATP-Mg salt, 0.3 GTP-Na salt, and 10 phosphocreatine. Recordings were made using a Multiclamp 700B amplifier whose output was digitized at 10 kHz (Digidata 1440A). Series resistance was <25 MΩ and was compensated up to 90%. Signals were analyzed using Igor Pro (Wavemetrics). Neurons were targeted using interference contrast and epifluorescence to visualize fluorescent indicators previously expressed via viral injection. ChR2-expressing axon terminals were stimulated by 5-20 ms laser pulses (3-10 mW) from a 473 nm laser delivered via fiber optic inside the recording pipette (Optopatcher, A-M Systems). To confirm the direct nature of optogenetically evoked currents 2µM TTX (Tocris) and 100µM 4AP (Sigma-Aldrich) were added to the ACSF and perfused onto slices. To confirm that evoked currents were GABAergic, 10µM gabazine (Tocris) was applied. Pharmacological agents including were bath applied for 10 minutes before making recordings.

Data availability: The data that support the findings of this study are available from the co-corresponding authors upon request.

Code availability: All custom-written Matlab codes used in this study are available from the co-corresponding authors. The latest version of Autoencoded Vocal Analysis, the Python package used to generate, plot, and analyze latent features of mouse USVs, is freely available online: https://github.com/jackgoffinet/autoencoded-vocal-analysis.

QUANTIFICATION AND STATISTICAL ANALYSES

Statistics: Parametric, two-sided statistical comparisons were used in all analyses unless otherwise noted (alpha=0.05). No statistical methods were used to predetermine sample sizes. Error bars represent standard error of the mean unless otherwise noted. Mice were selected at random for inclusion into either experimental or control groups for optogenetic experiments. Mice were only excluded from analysis in cases in which viral injections were not targeted accurately, or in cases with absent or poor viral expression.

Acknowledgements: Thanks to Michael Booze and Bao-Xia Han for additional mouse husbandry, thanks to Jun Takatoh for help with HCR *in situ* hybridization, and thanks to Shengli Zhao for providing CANE-related viruses. This work is supported by NIH grants DC 013826 (to R.M.) and MH 117778 (to F.W. and R.M.).

Author contributions: VM, KAT, JP, FW, and RM designed the experiments. VM and KAT conducted the experiments. VM, KAT, and JG analyzed data. VM, KAT, and RM wrote the manuscript, and all authors approved the final manuscript.

Competing interests: The authors declare no competing interests.

References

Alger, S.J., and Riters, L.V. (2006). Lesions to the medial preoptic nucleus differentially affect singing and nest box-directed behaviors within and outside of the breeding season in European starlings (Sturnus vulgaris). Behav Neurosci *120*, 1326-1336.

Balthazart, J., and Ball, G.F. (2007). Topography in the preoptic region: differential regulation of appetitive and consummatory male sexual behaviors. Front Neuroendocrinol *28*, 161-178.

Bandler, R., and Shipley, M.T. (1994). Columnar organization in the midbrain periaqueductal gray: modules for emotional expression? Trends Neurosci *17*, 379-389.

Bean, N.Y., Nunez, A.A., and Conner, R. (1981). Effects of medial preoptic lesions on male mouse ultrasonic vocalizations and copulatory behavior. Brain Res Bull *6*, 109-112.

Bennett, P.J.G., Maier, E., and Brecht, M. (2019). Involvement of rat posterior prelimbic and cingulate area 2 in vocalization control. Eur J Neurosci *50*, 3164-3180.

Campi, K.L., Jameson, C.E., and Trainor, B.C. (2013). Sexual Dimorphism in the Brain of the Monogamous California Mouse (Peromyscus californicus). Brain Behav Evol *81*, 236-249.

Cao, J., and Patisaul, H.B. (2013). Sexually dimorphic expression of hypothalamic estrogen receptors a and β and Kiss1 in neonatal male and female rats. J Comp Neurol *519*, 10.1002/cne.22648.

Carrive, P. (1993). The periaqueductal gray and defensive behavior: functional representation and neuronal organization. Behav Brain Res *58*, 27-47.

Chabout, J., Sarkar, A., Dunson, D.B., and Jarvis, E.D. (2015). Male mice song syntax depends on social contexts and influences female preferences. Front Behav Neurosci *9*, 76.

Chen, P., and Hong, W. (2018). Neural circuit mechanisms of social behavior. Neuron *98*, 16-30.

Clyne, J.D., and Miesenbock, G. (2008). Sex-specific control and tuning of the pattern generator for courtship song in Drosophila. Cell *133*, 354-363.

Dujardin, E., and Jurgens, U. (2006). Call type-specific differences in vocalization-related afferents to the periaqueductal gray of squirrel monkeys (Saimiri sciureus). Behav Brain Res *168*, 23-36.

Duvarci, S., and Pare, D. (2014). Amygdala microcircuits controlling learned fear. Neuron *82*, 966-980.

Ehrlich, I., Humeau, Y., Grenier, F., Ciocchi, S., Herry, C., and Luthi, A. (2009). Amygdala inhibitory circuits and the control of fear memory. Neuron *62*, 757-771.

Evans, D.A., Stempel, A.V., Vale, R., Ruehle, S., Lefler, Y., and Branco, T. (2018). A synaptic threshold mechanism for computing escape decisions. Nature *558*, 590-594.

Fang, Y.Y., Yamaguchi, T., Song, S.C., Tritsch, N.X., and Lin, D. (2018). A Hypothalamic Midbrain Pathway Essential for Driving Maternal Behaviors. Neuron *98*, 192-207 e110.

Fecteau, S., Belin, P., Joanette, Y., and Armony, J.L. (2007). Amygdala responses to nonlinguistics emotional vocalizations. Neuroimage *36*, 480-487.

Fenzl, T., and Schuller, G (2002). Periaqueductal gray and the region of the paralemniscal area have different functions in the control of vocalization in the neotropical bat, Phyllostomus discolor. Eur J Neurossci *16*, 1974-1986.

Floody, O.R. (1989). Dissociation of hypothalamic effects on ultrasound production and copulation. Physiol Behav *46*, 299-307.

Floody, O.R. (2009). Effects on hamster vocalization and aggression of carbachol injections into the MPOA/AH. Physiol Behav *96*, 294-299.

Floody, O.R., Cooper, T.T., and Albers, H.E. (1998). Injection of oxytocin into the medial preoptic-anterior hypothalamus increases ultrasound production by female hamsters. Peptides *19*, 833-839.

Forcelli, P.A., Waguespack, H.F., and Malkova, L. (2017). Defensive Vocalizations and Motor Asymmetry Triggered by Disinhibition of the Periaqueductal Gray in Non-human Primates. Front Neurosci *11*, 163.
Fu, X.W., and Brudzynski, S.M. (1994). High-frequency ultrasonic vocalization induced by intracerebral glutamate in rats. Pharmacol Biochem Behav *49*, 835-841.
Gadziola, M.A., Shanbhag, S.J., and Wenstrup, J.J. (2016). Two distinct representations of social vocalizations in the basolateral amygdala. J Neurophysiol 115, 868-886.
Gao, S.C., Wei, Y.C., Wang, S.R., and Xu, X.H. (2019). Medial Preoptic Area Modulates Courtship Ultrasonic Vocalization in Adult Male Mice. Neurosci Bull *35*, 697-708.
Goffinet, J., Mooney, R., Pearson, J. (2019). Inferring low-dimensional latent descriptions of animal vocalizations. bioRxiv.
Gorski, R.A., Gordon, J.H., Shryne, J.E., and Southam, A.M. (1978). Evidence for a morphological sex difference within the medial preoptic area of the rat brain. Brain Res *148*, 333-346.
Gothard, K. (2020). Multidimensional processing in the amygdala. Nat Rev Neurosci *21*, 565-575.
Green, D.B., Shackleton, T.M., Grimsley, J.M.S., Zobay, O., Palmer, A.R., and Wallace, M.N. (2018). Communication calls produced by electrical stimulation of four structures in the guinea pig brain. PLoS One *13*, e0194091.
Gretton, A., Borgwardt, K.M., Rasch, M.J., Scholkopf, B., Smola, A. (2012). A Kernel Two-Sample Test. Journal of Machine Learning Research *13*, 723-773.
Hall, I.C., Ballagh, I.H., and Kelley, D.B. (2013). The Xenopus amygdala mediates socially appropriate vocal communication signals. J. Neurosci. *33,* 14534-14548.
Hanson, J.L., and Hurley, L.M. (2012). Female presence and estrous state influence mouse ultrasonic courtship vocalizations. PLoS One *7*, e40782.
Holstege, G. (2014). The periaqueductal gray controls brainstem emotional motor systems including respiration. Prog Brain Res *209*, 379-405.
Holy, T.E., and Guo, Z. (2005). Ultrasonic songs of male mice. PLoS Biol *3*, e386.
Janak, P.H., and Tye, K.M. (2015). From circuits to behaviour in the amygdala. Nature *517*, 284-292.
Jurgens, U. (1982). Amygdalar vocalization pathways in the squirrel monkey. Brain Res *241*, 189-196.
Jurgens, U. (1994). The role of the periaqueductal grey in vocal behaviour. Behav Brain Res *62*, 107-117.
Jurgens, U. (2002). Neural pathways underlying vocal control. Neurosci Biobehav Rev *26*, 235-258.
Jurgens, U. (2009). The neural control of vocalization in mammals: a review. J Voice *23*, 1-10.
Jurgens, U., and Ploog, D. (1970). Cerebral representation of vocalization in the squirrel monkey. Exp Brain Res *10*, 532-554.
Jurgens, U., and Pratt, R. (1979). Role of the periaqueductal grey in vocal expression of emotion. Brain Res *167*, 367-378.
Jurgens, U., and Richter, K. (1986). Glutamate-induced vocalization in the squirrel monkey. Brain Res *373*, 349-358.
Keesom, S.M., Finton, C.J., Sell, G.L., and Hurley, L.M. (2017). Early-Life Social Isolation Influences Mouse Ultrasonic Vocalizations during Male-Male Social Encounters. PLoS One *12*, e0169705.
Kingma, D.P., Welling, M. (2013). Auto-Encoding Variational Bayes. ArXiv.
Kohl, J., Babayan, B.M., Rubinstein, N.D., Autry, A.E., Marin-Rodriguez, B., Kapoor, V., Miyamishi, K., Zweifel, L.S., Luo, L., Uchida, N.*, et al.* (2018). Functional circuit architecture underlying parental behaviour. Nature *556*, 326-331.

Kyuhou, S., and Gemba, H. (1998). Two vocalization-related subregions in the midbrain periaqueductal gray of the guinea pig. Neuroreport *9*, 1607-1610.
LeDoux, J. (2007). The amygdala. Curr Biol *17*, R868-874.
Lenz, K.M., Nugent, B.M., and McCarthy, M.M. (2012). Sexual differentiation of the rodent brain: dogma and beyond. Front Neurosci *6:26*, doi: 10.3389/fnins.2012.00026
Lin, D., Boyle, M.P., Dollar, P., Lee, H., Perona, P., Lein, E.S., and Anderson, D.J. (2011). Functional identification of an aggression locus in the mouse hypothalamus. Nature *470*, 221-226.
Lu, C.L., and Jurgens, U. (1993). Effects of chemical stimulation in the periaqueductal gray on vocalization in the squirrel monkey. Brain Res Bull *32*, 143-151.
Ma, J., and Kanwal, J.S. (2014). Stimulation of the basal and central amygdala in the mustached bat triggers echolocation and agonistic vocalizations within multimodal output. Front Physiol *5*, 55.
Maggio, J.C., and Whitney, G. (1985). Ultrasonic vocalizing by adult female mice (Mus musculus). J Comp Psychol *99*, 420-436.
Manteuffel, G., Schon, P.C., Dupjan, S., Tuchscherer, A., and Bellmann, O. (2007). Acetylcholine injection into the amygdala elicits vocalization in domestic pigs (Sus scrofa). Behav Brain Res *178*, 177-180.
Matsumoto, Y.K., Okanoya, K., and Seki, Y. (2012). Effects of amygdala lesions on male mouse ultrasonic vocalizations and copulatory behaviour. Neuroreport *23*, 676-680.
Matsumoto, Y.K., and Okanoya, K. (2016). Phase-Specific Vocalizations of Male Mice at the Initial Encounter during the Courtship Sequence. PLoS One *11*, e0147102.
McInnes, L., Healy, J., Melville, J. (2018). UMAP: Uniform Manifold Approximation and Projection for Dimension Reduction. arXiv.
McKinsey, G., Ahmed, O.M., and Shah, N.M. (2018). Neural control of sexually dimorphic social behaviors. Curr Opin Physiol *6*, 89-95.
Moffitt, J.R., Bambah-Mukku, D., Eichhorn, S.W., Vaughn, E., Shekhar, K., Perez, J.D., Rubinstein, N.D., Hao, J., Regev, A., Dulac, C.*, et al.* (2018). Molecular, spatial, and functional single-cell profiling of the hypothalamic preoptic region. Science *362*.
Morgan, M.M., and Clayton, C.C. (2005). Defensive behaviors evoked from the ventrolateral periaqueductal gray of the rat: comparison of opioid and GABA disinhibition. Behav Brain Res *164*, 61-66.
Neunuebel, J.P., Taylor, A.L., Arthur, B.J., and Egnor, S.E. (2015). Female mice ultrasonically interact with males during courtship displays. Elife *4*.
Newman, S.W. (1999). The medial extended amygdala in male reproductive behavior. A node in the mammalian social behavior network. Ann N Y Acad Sci *877*, 242-257.
Nyby, J., Wysocki, C.J., Whitney, G., Dizinno, G., and Schneider, J. (1979). Elicitation of male mouse (Mus muscululs) ultrasonic vocalization: 1. Urinary Cues. Journal of Comparative and Physiological Psychology *93*, 957-975.
Orikasa, C., and Sakuma, Y. (2010). Estrogen configures sexual dimorphism in the preoptic area of C57BL/6J and ddN strains of mice. J Comp Neurol *518*, 3618-3629.
Panzica, G.C., Viglietti-Panzica, C., and Balthazart, J. (1996). The sexually dimorphic medial preoptic nucleus of quail: a key brain area mediating steroid action on male sexual behavior. Front Neuroendocrinol *17*, 51-125.
Portfors, C.V., and Perkel, D.J. (2014). The role of ultrasonic vocalizations in mouse communication. Curr Opin Neurobiol *28*, 115-120.
Raisman, G., and Field, P.M. (1971). Sexual dimorphism in the preoptic area of the rat. Science *173*, 731-733.
Rezaval, C., Pattnaik, S., Pavlou, H.J., Nojima, T., Bruggemeier, B., D'Souza, L.A.D., Dweck, H.K.M., and Goodwin, S.F. (2016). Activation of Latent Courtship Circuitry in the Brain of Drosophila Females Induces Male-like Behaviors. Curr Biol *26*, 2508-2515.

Riters, L.V., and Ball, G.F. (1999). Lesions to the medial preoptic area affect singing in the male European starling (Sturnus vulgaris). Horm Behav *36*, 276-286.
Rodriguez, E., Sakurai, K., Xu, J., Chen, Y., Toda, K., Zhao, S., Han, B.X., Ryu, D., Yin, H., Liedtke, W.*, et al.* (2017). A craniofacial-specific monosynaptic circuit enables heightened affective pain. Nat Neurosci *20*, 1734-1743.
Sainburg, T., Theilman, B., Thielk, M., and Gentner, T.Q. (2019). Parallels in the sequential organization of birdsong and human speech. Nat Commun *10*, 3636.
Sakurai, K., Zhao, S., Takatoh, J., Rodriguez, E., Lu, J., Leavitt, A.D., Fu, M., Han, B.X., and Wang, F. (2016). Capturing and Manipulating Activated Neuronal Ensembles with CANE Delineates a Hypothalamic Social-Fear Circuit. Neuron *92*, 739-753.
Schönfeld, L.M., Zech, M.P., Schäble, S., Wöhr, M., and Kalenscher, T. (2020). Lesions of the rat basolateral amygdala reduce the behavioral response to ultrasonic vocalizations. Behav Brain Res *378*, 112274.
Siebert, S., and Jurgens, U. (2003). Vocalization after periaqueductal grey inactivation with the GABA agonist muscimol in the squirrel monkey. Neurosci Lett *340*, 111-114.
Sternson, S.M. (2013). Hypothalamic survival circuits: blueprints for purposive behaviors. Neuron *77*, 810-824.
Stivers, T., Enfield, N. J., Brown, P., Englert, C., Hayashi, M., Heinemann, T., Hoymann, G., Rossano, F., de Ruiter, J.P., Yoon, K.E., and Levinson, S.C. (2009). Universals and cultural variation in turn-taking in conversation. Proc Natl Acad Sci U.S.A. *106*, 10587–10592.
Subramanian, ,H.H., Balnave, R.J., and Holstege, G. (2020). Microstimulation in different parts of the periaqueductal gray generates different types of vocalizations in the cat. J Voice *S0892-1997*, 30589-2.
Sugiyama, Y., Shiba, K., Nakazawa, K., Suzuki, T., and Hisa, Y. (2010). Brainstem vocalization area in guinea pigs. Neuroscie Res *66*, 359-65.
Tovote, P., Esposito, M.S., Botta, P., Chaudun, F., Fadok, J.P., Markovic, M., Wolff, S.B., Ramakrishnan, C., Fenno, L., Deisseroth, K.*, et al.* (2016). Midbrain circuits for defensive behaviour. Nature *534*, 206-212.
Tschida, K., Michael, V., Takatoh, J., Han, B.X., Zhao, S., Sakurai, K., Mooney, R., and Wang, F. (2019). A Specialized Neural Circuit Gates Social Vocalizations in the Mouse. Neuron *103*, 459-472 e454.
Van Segbroeck, M., Knoll, A.T., Levitt, P., and Narayanan, S. (2017). MUPET-Mouse Ultrasonic Profile ExTraction: A Signal Processing Tool for Rapid and Unsupervised Analysis of Ultrasonic Vocalizations. Neuron *94*, 465-485 e465.
Vandries, L.M., Ghorbanpoor, S., Cornez, G., Shevchouk, O.T., Ball, G.F., Cornil, C.A., and Balthazart, J. (2019). Testosterone or Estradiol When Implanted in the Medial Preoptic Nucleus Trigger Short Low-Amplitude Songs in Female Canaries. eNeuro *6*.
Wei, Y.C., Wang, S.R., Jiao, Z.L., Zhang, W., Lin, J.K., Li, X.Y., Li, S.S., Zhang, X., and Xu, X.H. (2018). Medial preoptic area in mice is capable of mediating sexually dimorphic behaviors regardless of gender. Nat Commun *9*, 279.
White, N.R., Prasad, M., Barfield, R.J., and Nyby, J.G. (1998). 40- and 70-kHz vocalizations of mice (Mus musculus) during copulation. Physiol Behav *63*, 467-473.
Whitney, G., Alpern, M., Dizinno, G., and Horowitz, G. (1974). Female odors evoke ultrasounds from male mice. Anim Learn Behav *2*, 13-18.
Wu, Z., Autry, A.E., Bergan, J.F., Watabe-Uchida, M., and Dulac, C.G. (2014). Galanin neurons in the medial preoptic area govern parental behaviour. Nature *509*, 325-330.
Xu, X., Coats, J.K., Yang, C.F., Wang, A., Ahmed, O.M., Alvarado, M., Izumi, T., and Shah, N.M. (2012). Modular genetic control of sexually dimorphic behaviors. Cell *148*, 596-607.

Figure 1. Inhibitory neurons in the hypothalamus and amygdala provide input to the PAG vocal gating circuit

A Monosynaptic Inputs to PAG-USV neurons (N=4 mice)

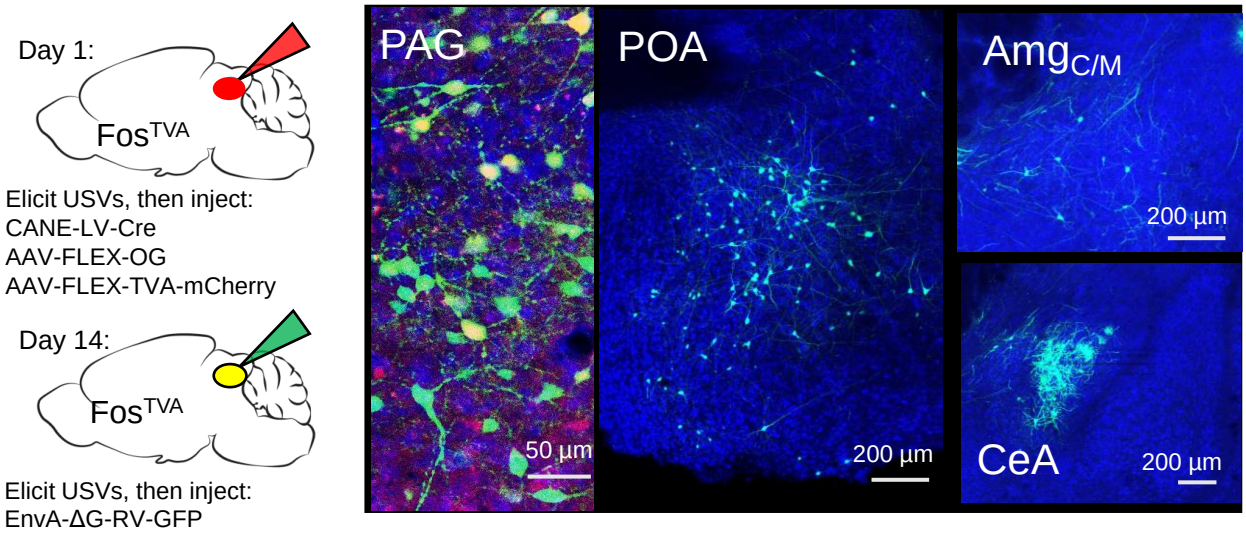

B Monosynaptic Inputs to PAG-VGAT^{+} neurons (N=6 mice)

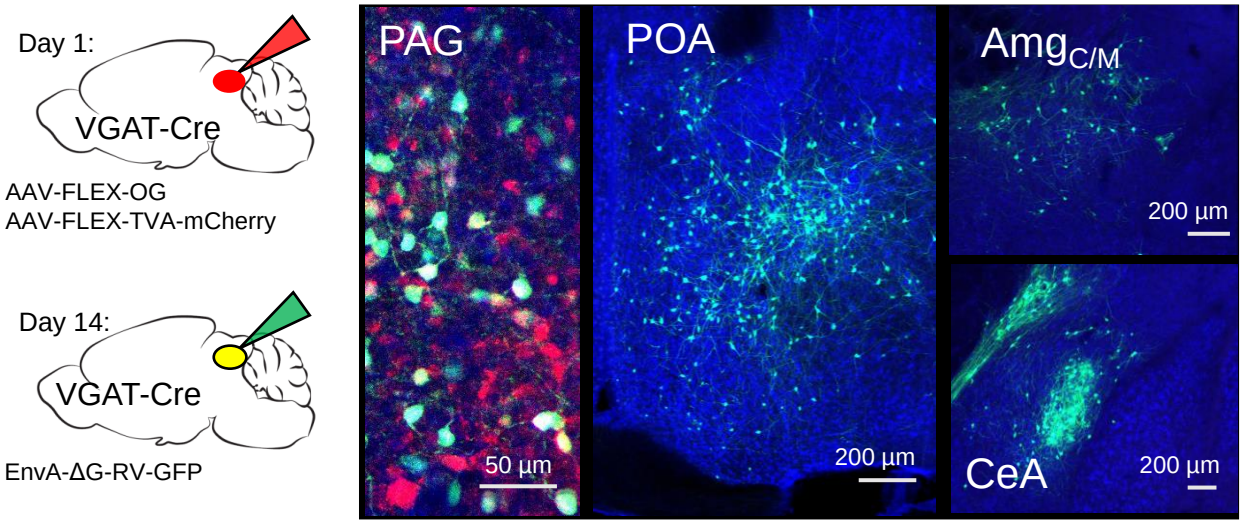

C POA inputs to PAG-VGAT^{+} neurons

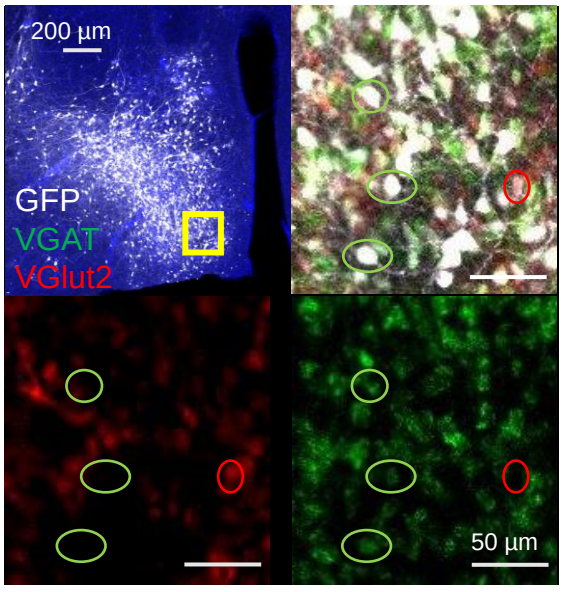

D

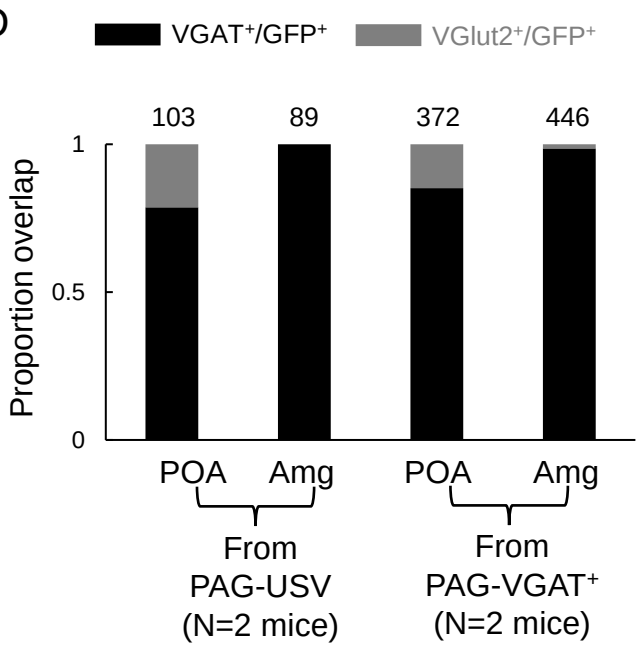

Figure 1: Inhibitory neurons in the hypothalamus and amygdala provide input to the PAG vocal gating circuit. (A) (Left) Viral strategy shown for transsynaptic labeling of direct inputs to PAG-USV neurons (performed in N=4 males). (Right) Confocal images are shown of starter PAG-USV neurons, upstream neurons labeled within the POA, and upstream neurons labeled within the $Amg_{C/M}$ and CeA (B) Same, for transsynaptic labeling of direct inputs to GABAergic PAG neurons (performed in N=4 males, N=2 females). (C) Representative confocal image of in situ hybridization performed on transsynaptically-labeled POA neurons that provide direct input to GABAergic PAG neurons (labeled with GFP, shown in white), showing overlap with expression of VGAT (green) and VGlut2 (red). DAPI shown in blue. (D) Quantification of overlap of transsynaptically labeled POA and amygdala neurons (CeA and $Amg_{C/M}$ combined) with VGAT and VGlut2 (N=2 male mice per condition). Total numbers of neurons scored for overlap in each condition are indicated by the numbers over the bars. See also Table S1 and Figures S1-4.

Figure 2. Activating PAG-projecting POA neurons elicits USVs in the absence of social cues

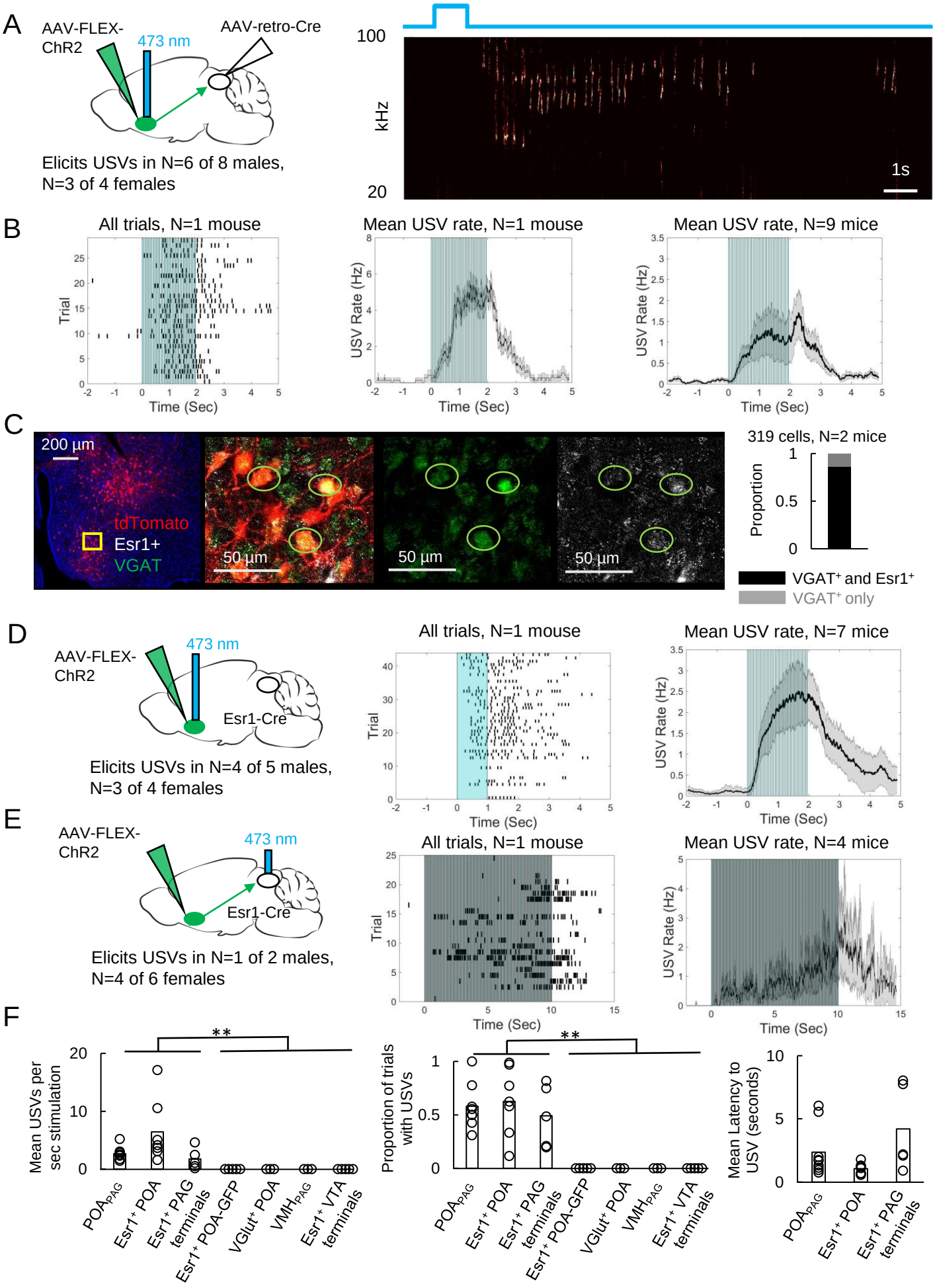

Figure 2: Activating PAG-projecting POA neurons elicits USVs in the absence of social cues. (A) (Left) Viral strategy to express ChR2 in POA_{PAG} neurons. (Right) Example trial showing that optogenetic activation of POA_{PAG} neurons elicits USV production in an isolated animal. (B) (Left) Raster plot shows USVs elicited in many trials in a representative mouse following optogenetic activation of POA_{PAG} neurons. (Middle) Mean USV rate aligned to delivery of blue light pulses plotted for that same mouse. (Right) Mean USV rate plotted for N=9 mice following optogenetic activation of POA_{PAG} neurons. (C) Representative confocal image and quantification of in situ hybridization performed on POA_{PAG} neurons (tdTomato, red), showing overlap with Esr1 (white) and VGAT (green). DAPI is blue, N=2 mice. (D) (Left) Viral strategy used to express ChR2 in $Esr1^+$ POA neurons. (Middle) Raster plot shows USVs elicited in many trials in a representative mouse following optogenetic activation of $Esr1^+$ POA neurons. (Right) Mean USV rate plotted for N=7 mice following optogenetic activation of $Esr1^+$ POA neurons. (E) Same as (D), for experiments in which the axon terminals of $Esr1^+$ POA neurons were optogenetically activated within the PAG. Data shown for stimulation with10s-long, 20 Hz blue light pulses. Please note that one mouse in which USVs were elicited by optogenetic stimuli that did not include the 10s-long, 20 Hz stimulus is excluded from the summary analysis shown in the right-most panel. See also Figures S5, S6, and S9. (F) Summary plots show mean number of USVs per second of optogenetic stimulation (left, p=0.0013, one-way ANOVA between all groups, with post-hoc t-tests showing that each experimental condition was significantly different from control conditions at p<.01), mean number of optogenetic trials with USVs (middle, p=1.8E-6, one-way ANOVA between all groups, with post-hoc t-tests showing that each experimental condition was significantly different from control conditions at p<.01), and mean latency from onset of optogenetic stimulus to onset of first USV (right) for mice in which optogenetic stimulation was applied to POA_{PAG} neurons (N=9 mice), $Esr1^+$ POA neurons (N=7 mice), $Esr1^+$ POA axon terminals within the PAG (N=5 mice), GFP-expressing $Esr1^+$ POA neurons (N=5 mice), $VGlut^+$ POA neurons (N=3 mice), VMH_{PAG} neurons (N=3), and Esr1+ POA axon terminals within the VTA (N=4 mice).

Figure 3. Acoustic characterization of USVs elicited by optogenetic activation of POA neurons

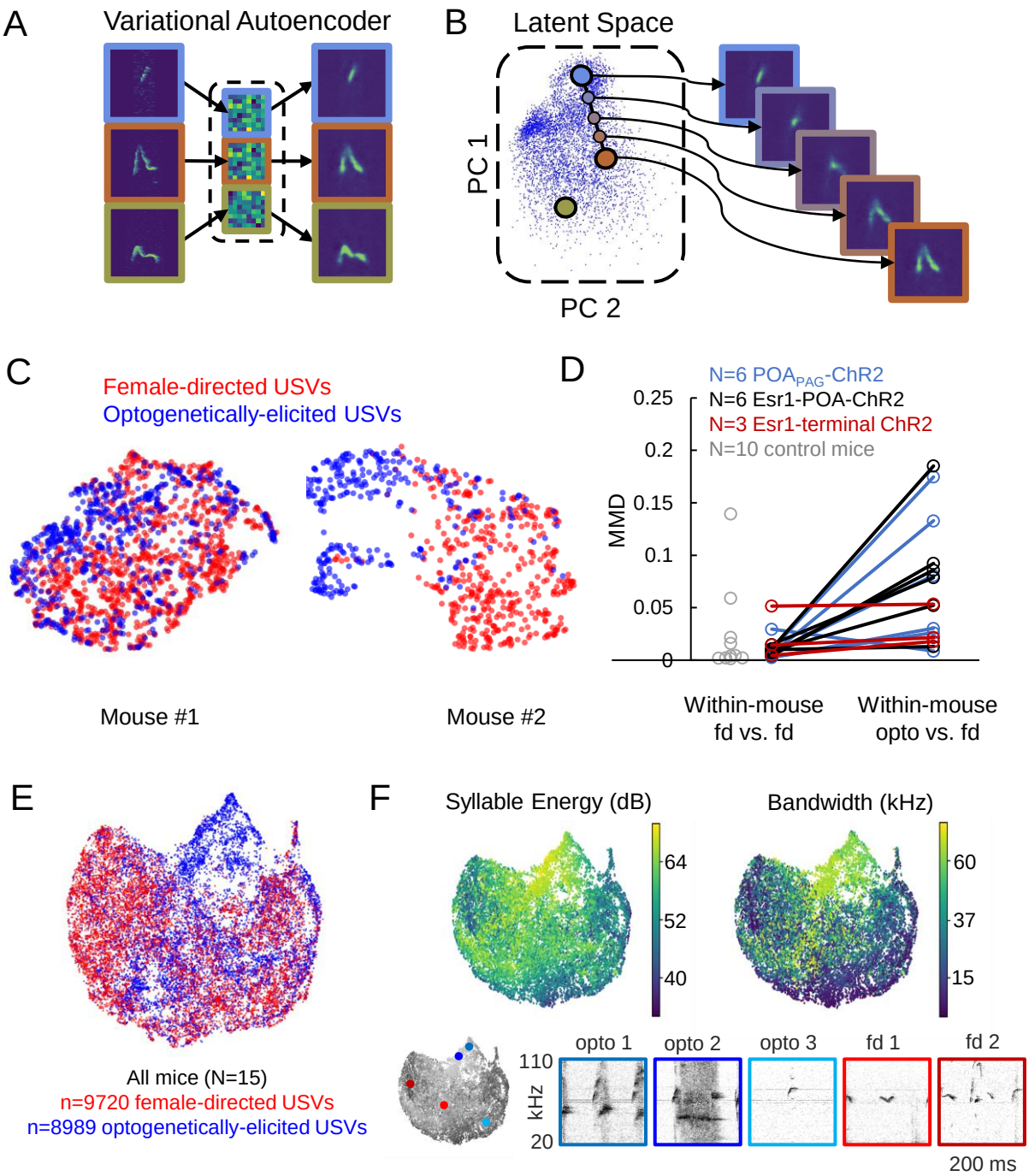

Figure 3: Acoustic characterization of USVs elicited by optogenetic activation of POA neurons. (A) The VAE takes spectrograms as input (left), maps the spectrograms to low-dimensional latent representations using an encoder (middle), and approximately reconstructs the input spectrogram using a decoder (right). (B) (Left) Dimensionality reduction techniques such as PCA or UMAP can be used to visualize the resulting latent vectors. (Right) Interpolations in latent space correspond to smooth USV syllable changes in spectrogram space exhibiting realistic dimensions of variation. (C) UMAP projections of latent syllable representations of female-directed USVs (red) and optogenetically-elicited USVs (blue) from two example mice. (D) MMD was calculated between distributions of latent syllable representations to generate three comparisons: female-directed USVs from the first half of the recording session vs. female-directed USVs from the second half, all female-directed USVs vs. opto-USVs (N=16 experimental mice), and female-directed USVs from two different recordings sessions in N=10 control mice (gray points). Note that larger MMD values indicate that distributions are more dissimilar (E) UMAP projections of latent descriptions of female-directed (red) and optogenetically-elicited USVs (blue) for all mice (N=15). (F) UMAP projections of optogenetically-elicited USVs only, color-coded by total energy (left) and frequency bandwidth (right). Example spectrograms of opto-USVS and female-directed USVs are plotted below, and the location of each example USV in UMAP space is indicated by the colored dots on the grayscale UMAP projection on the bottom left.

Figure 4: Activation of $Amg_{C/M-PAG}$ neurons transiently suppresses USV production

A

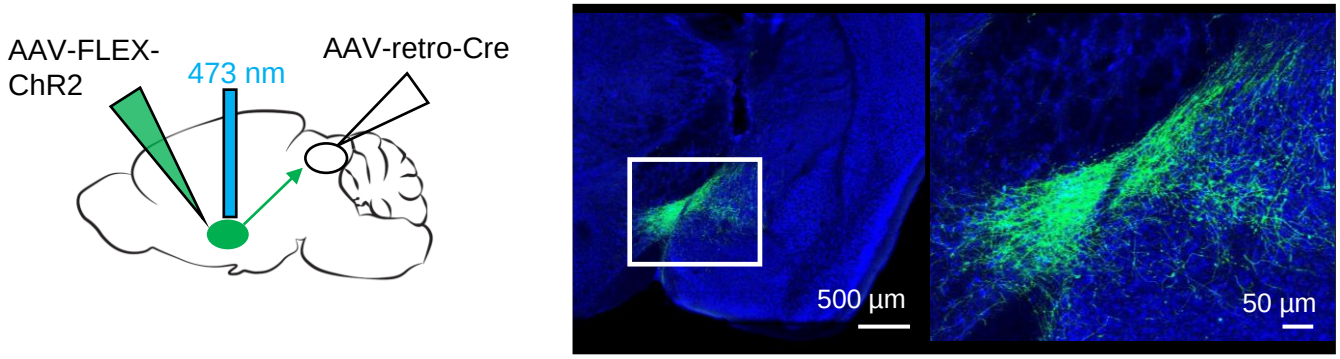

B

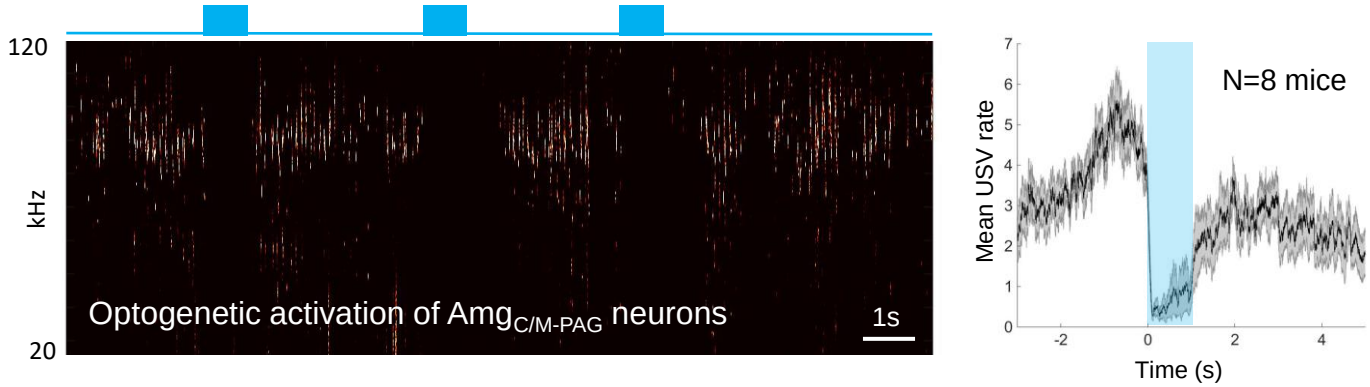

C

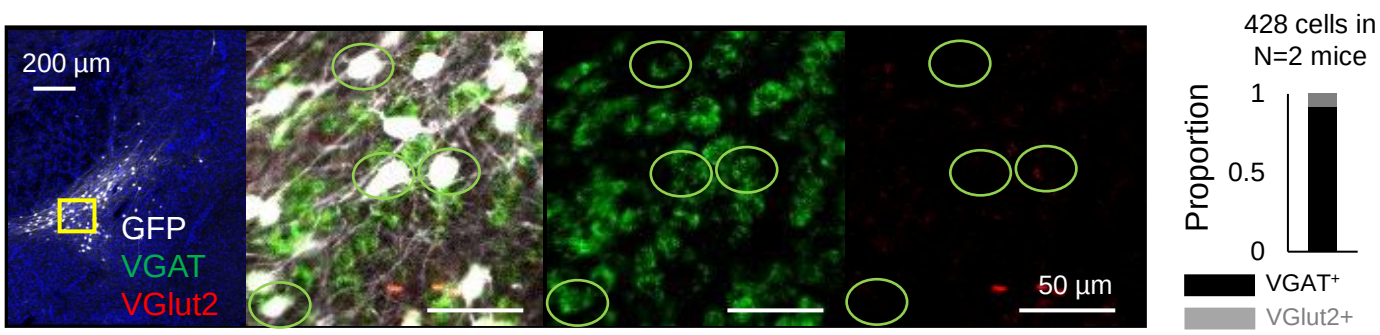

D

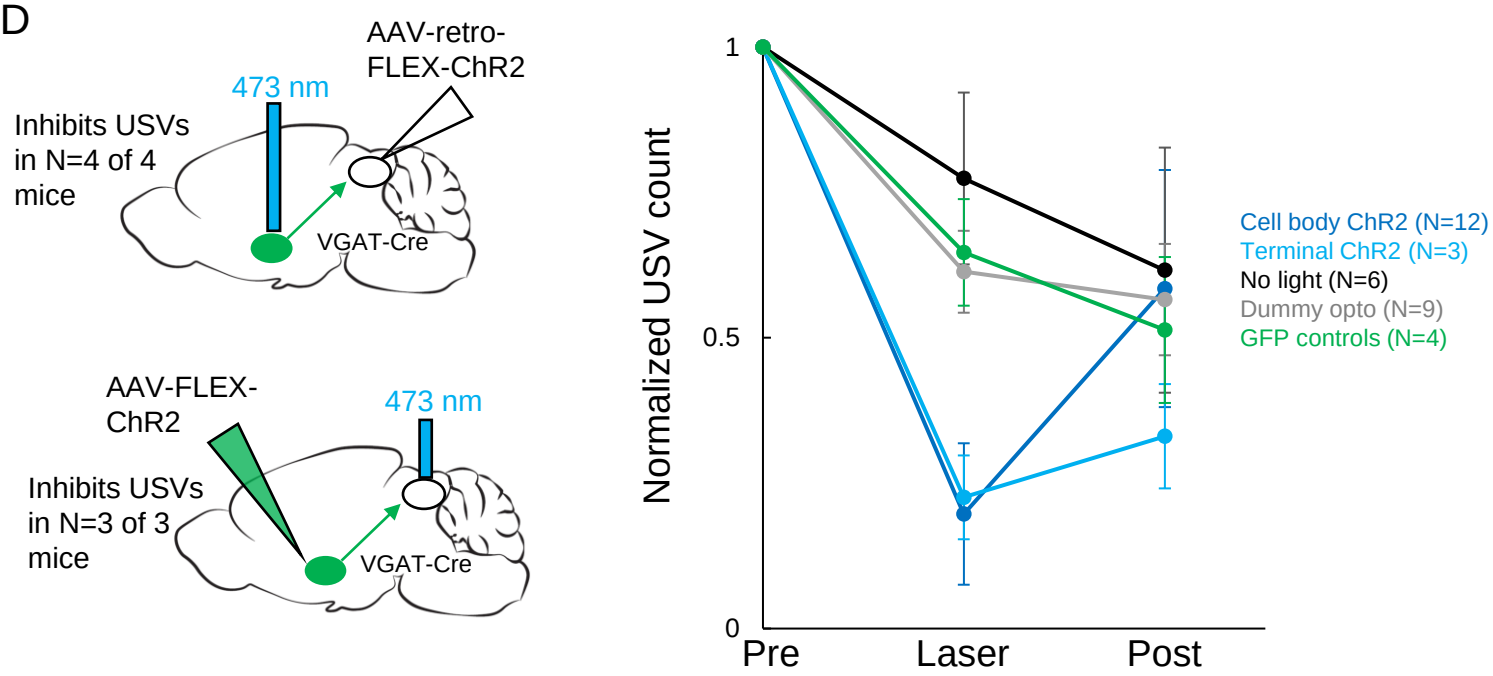

Figure 4: Activating $Amg_{C/M-PAG}$ neurons transiently suppresses USV production. (A) (Left) Viral strategy used to express ChR2 in $Amg_{C/M-PAG}$ neurons. (Right) Confocal image of representative $Amg_{C/M-PAG}$ cell body labeling achieved with this viral strategy. (B) (Left) Spectrogram showing a representative trial in which optogenetic activation of $Amg_{C/M-PAG}$ neurons suppresses USV production during the laser stimulation period. (Right) Group data quantified for N=8 mice. (C) Confocal image and quantification of in situ hybridization performed on $Amg_{C/M-PAG}$ neurons (GFP, shown in white), showing overlap with VGlut2 (red) and VGAT (green). DAPI in blue, N=2 mice. (D) Left: viral strategy used to express ChR2 in the PAG axon terminals of $Amg_{C/M-PAG}$ neurons. Right: Quantification of the number of USVs produced in the 1s period prior to optogenetic stimulation (pre), the 1s period of optogenetic stimulation (laser), and the 1s period following optogenetic stimulation (post). Data for each mouse were normalized by dividing the pre, laser, and post measurements by the total number of USVs produced during the pre-laser period. Group averages are shown for mice in which $Amg_{C/M-PAG}$ neurons were optogenetically activated (N=12, dark blue), mice in which the PAG axon terminals of $Amg_{C/M-PAG}$ neurons were optogenetically activated (N=3, light blue), control mice in which the blue laser was shined over the mouse's head but not connected to the optogenetic ferrule (N=9, gray), control mice in which GFP was expressed in $Amg_{C/M-PAG}$ neurons (N=4, green), and control mice in which the laser was triggered but not turned on (N=6, black). Error bars represent S.E.M. Please note that the decay in USV rates over time in the control groups reflects the natural statistics of USV production (increasing probability that a bout will end as time progresses). See also Figures S5, S7, S8, and S9.

Figure 5: $Amg_{C/M}$ neurons provide direct inhibition onto PAG-USV neurons

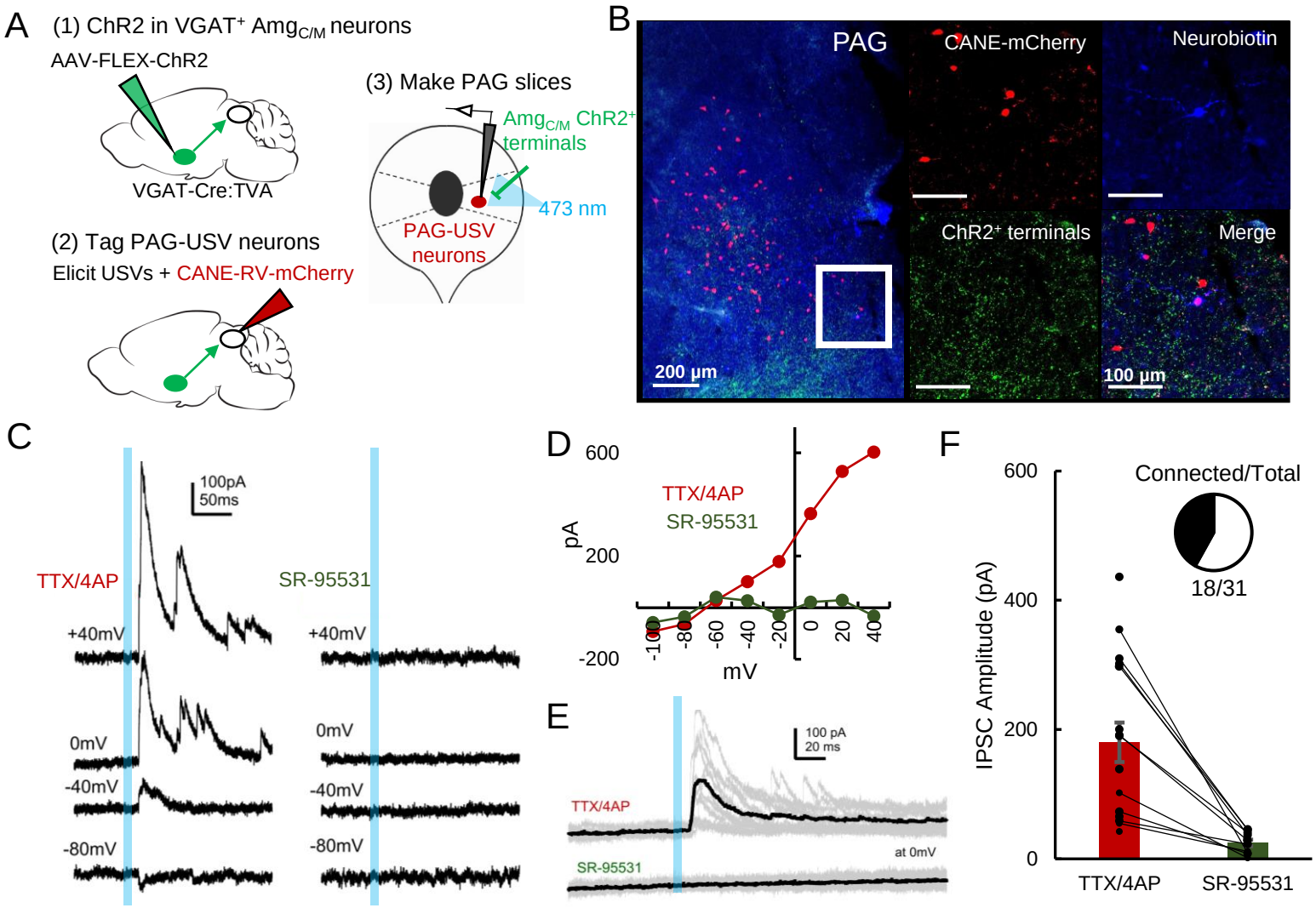

Figure 5: $Amg_{C/M}$ neurons provide direct inhibition onto PAG-USV neurons. (A) Viral strategy (left) and schematic (right) for whole-cell patch clamp recordings from fluorescently identified CANE-tagged PAG-USV neurons while optogenetically activating $Amg_{C/M\text{-}PAG}$ axons. (B) Example image of overlap of neurobiotin and mCherry-labeled PAG-USV cells with ChR2-expressing $Amg_{C/M\text{-}PAG}$ axon terminals in the PAG. (C) Example of light-evoked IPSCs at different voltages from one PAG-USV cell recorded in TTX/4AP while stimulating $Amg_{C/M\text{-}PAG}$ axons (left). IPSCs were abolished by bath gabazine application (right). (D) The peak magnitude of light-evoked currents at different membrane voltages for the same cell as (C) shows that the current reverses around the reversal potential of chloride and is abolished by gabazine. Currents were identified as IPSCs in this manner based on their reversal behavior and, for a subset of cells, by disappearance in gabazine. (E,F) Light-evoked IPSCs recorded in TTX/4AP (observed in n = 16 of 29 CANE-tagged cells from 9 mice) were abolished by application of gabazine (n = 10 cells also recorded in gabazine, N=10 cells, $p<0.001$, paired t-test). IPSC amplitude refers to the peak of the light-evoked current at 0 mV holding potential. Error bars represent S.E.M.

Figure 6: POA neurons provide direct inhibition onto VGAT⁺ PAG neurons, which provide direct inhibition onto PAG-USV neurons

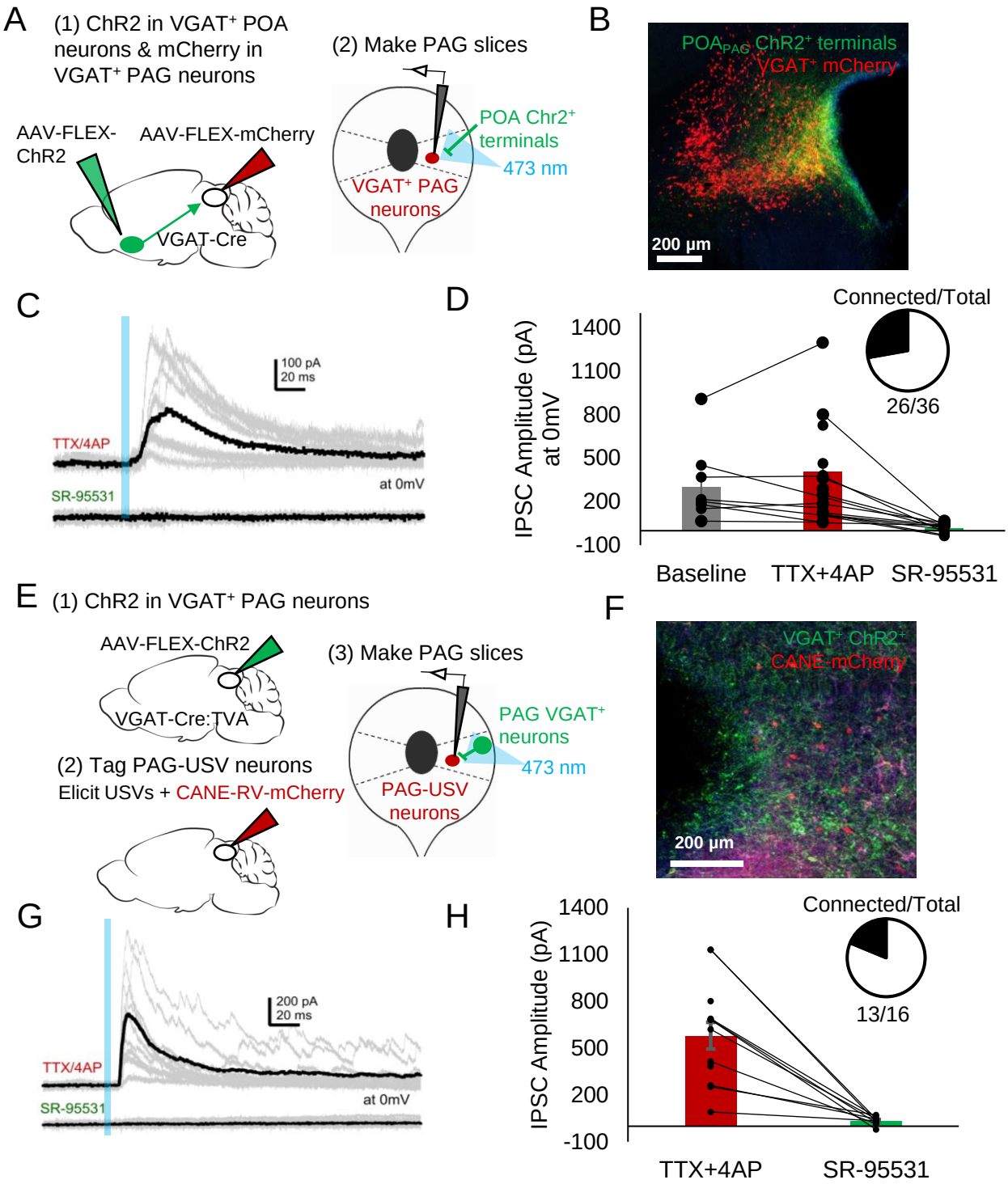

Figure 6: POA neurons provide direct inhibition onto VGAT$^+$ PAG neurons, which provide direct inhibition onto PAG-USV neurons. (A) Viral strategy (left) and schematic (right) for whole-cell patch clamp recordings from fluorescently identified VGAT$^+$ PAG cells while optogenetically activating POA_{PAG} axons. (B) Example image of mCherry-labeled VGAT$^+$ neurons with ChR2-labeled POA_{PAG} axon terminals in the PAG. (C, D) Light-evoked IPSCs (observed in n=26 of 36 VGAT$^+$ neurons recorded from 11 mice) persisted in TTX/4AP and were abolished by bath application of gabazine (n=10 cells recorded at baseline, n=22 cells recorded in TTX/4AP, and n=13 cells also recorded in gabazine including the following pairs: 6 cells recorded in both baseline and TTX/4AP, 3 cells recorded in both baseline and gabazine, and 10 cells recorded in both TTX/4AP and gabazine, p=0.03, one-way ANOVA comparing baseline vs. TTX+4-AP vs. SR-95531, followed by a post-hoc t-test revealing a significant difference between TTX+4-AP vs. SR-95531, p<.018). IPSC amplitude refers to the peak of the light-evoked current at 0 mV holding potential. Error bars represent S.E.M. (E) Viral strategy (left) and schematic (right) for whole-cell recordings from fluorescently identified CANE-tagged PAG-USV neurons while optogenetically activating local VGAT$^+$ PAG neurons. (F) Example image of mCherry-labeled CANE-tagged PAG-USV neurons and ChR2-labeled VGAT$^+$ PAG neurons. (G,H) Light-evoked IPSCs recorded in TTX/4AP (observed in n = 13 of 16 CANE-tagged cells from 4 mice) were abolished by gabazine application (N=10 cells also recorded in gabazine, p<0.001, paired t-test). IPSC amplitude refers to the peak of the light-evoked current at 0 mV holding potential. Error bars represent S.E.M. See also Figure S10.

Figure 7: Model of bidirectional descending control of the PAG vocal gating circuit

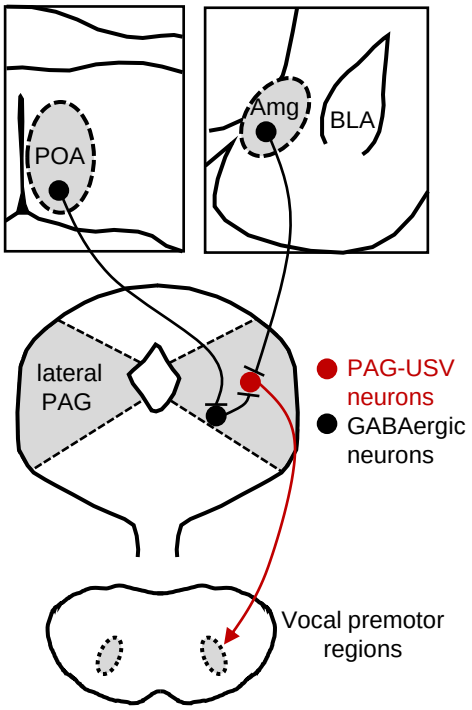

Figure 7: Model of bidirectional descending control of the PAG vocal gating circuit. Inhibitory neurons within the POA provide direct input to inhibitory neurons within the PAG, which in turn provide direct input to PAG-USV neurons. In this manner, activation of POA_{PAG} neurons disinhibits PAG-USV neurons, which provide excitatory input to downstream vocal premotor neurons and drive USV production. Conversely, inhibitory neurons within the $Amg_{C/M}$ provide direct inhibitory input to PAG-USV neurons. Hence activation of $Amg_{C/M\text{-}PAG}$ neurons reduces PAG-USV activity and transiently suppresses USV production.

Supplementary Information: We have included ten supplemental figures, three supplemental movies, and one supplemental table.

Figure S1, related to Figure 1: Monosynaptic rabies-based tracing reveals POA and amygdala inputs to the midbrain vocalization circuit.

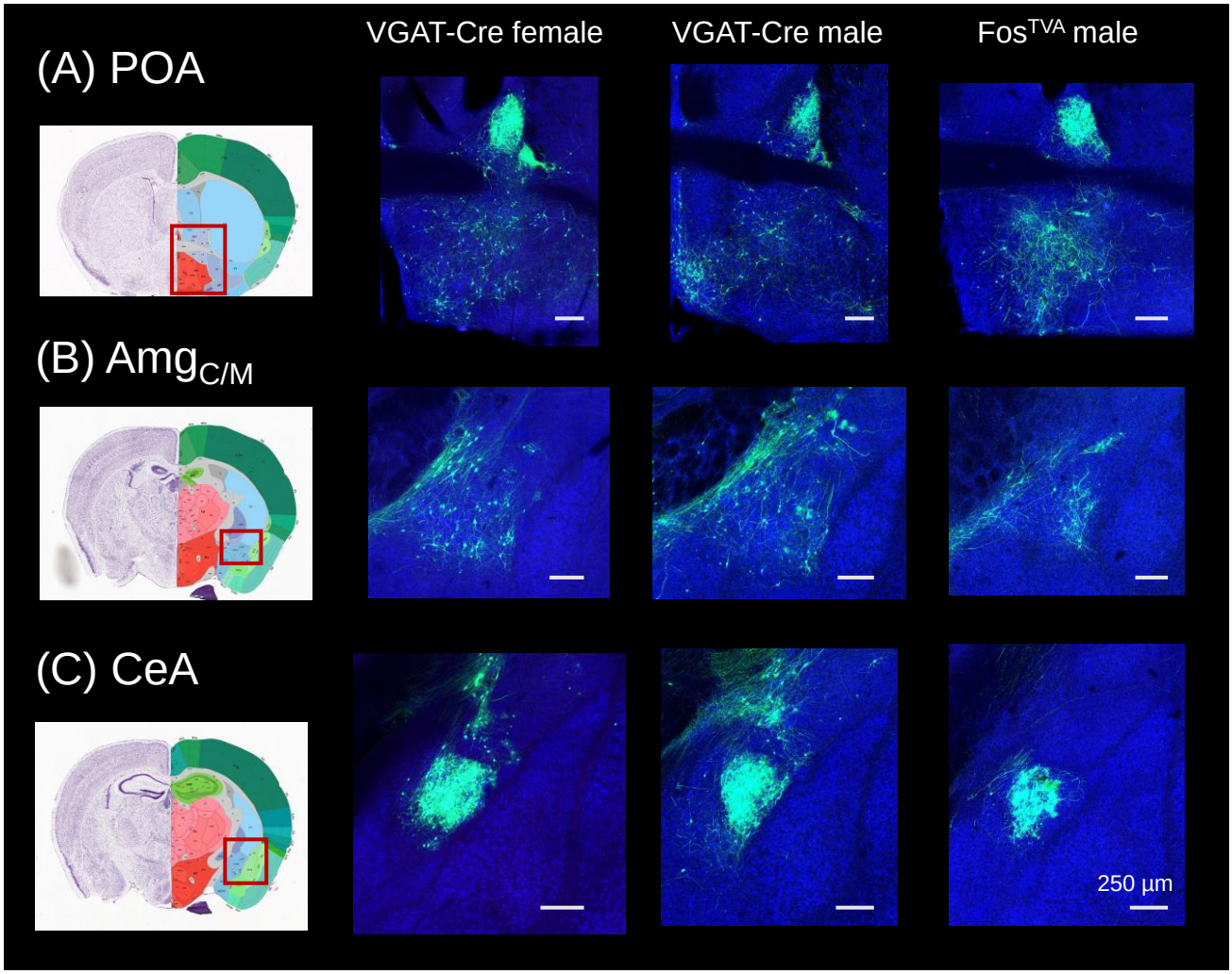

Figure S1, related to Figure 1: Monosynaptic rabies-based tracing reveals preoptic and amygdala inputs to the midbrain vocalization circuit. (A) Example confocal images showing transsynaptic labeling of neurons in the preoptic area of the hypothalamus (POA, green) that provide monosynaptic input to GABAergic PAG neurons (left-most confocal image, VGAT-Cre female; middle confocal image, VGAT-Cre male) or to PAG-USV neurons (right confocal image, Fos^{TVA} male; blue, Neurotrace). (B-C) Same, for transsynaptically labeled neurons in (B) the central-medial boundary region of the amygdala ($Amg_{C/M}$) and (C) the central amygdala (CeA). Coronal brain atlas images show the approximate plane of section of the confocal images to the right. Red rectangles superimposed on the atlas images indicate the approximate location of the brain regions shown in the confocal images. See also Table S1 and Figures S2-4. Scale bars, 250 µm. All brain atlas images were obtained from the Allen Mouse Brain Reference Atlas, (https://mouse.brain-map.org/experiment/thumbnails/100048576?Image_type=atlas).

Figure S2, related to Figure 1: Monosynaptic rabies-based tracing reveals cortical inputs to the midbrain vocalization circuit.

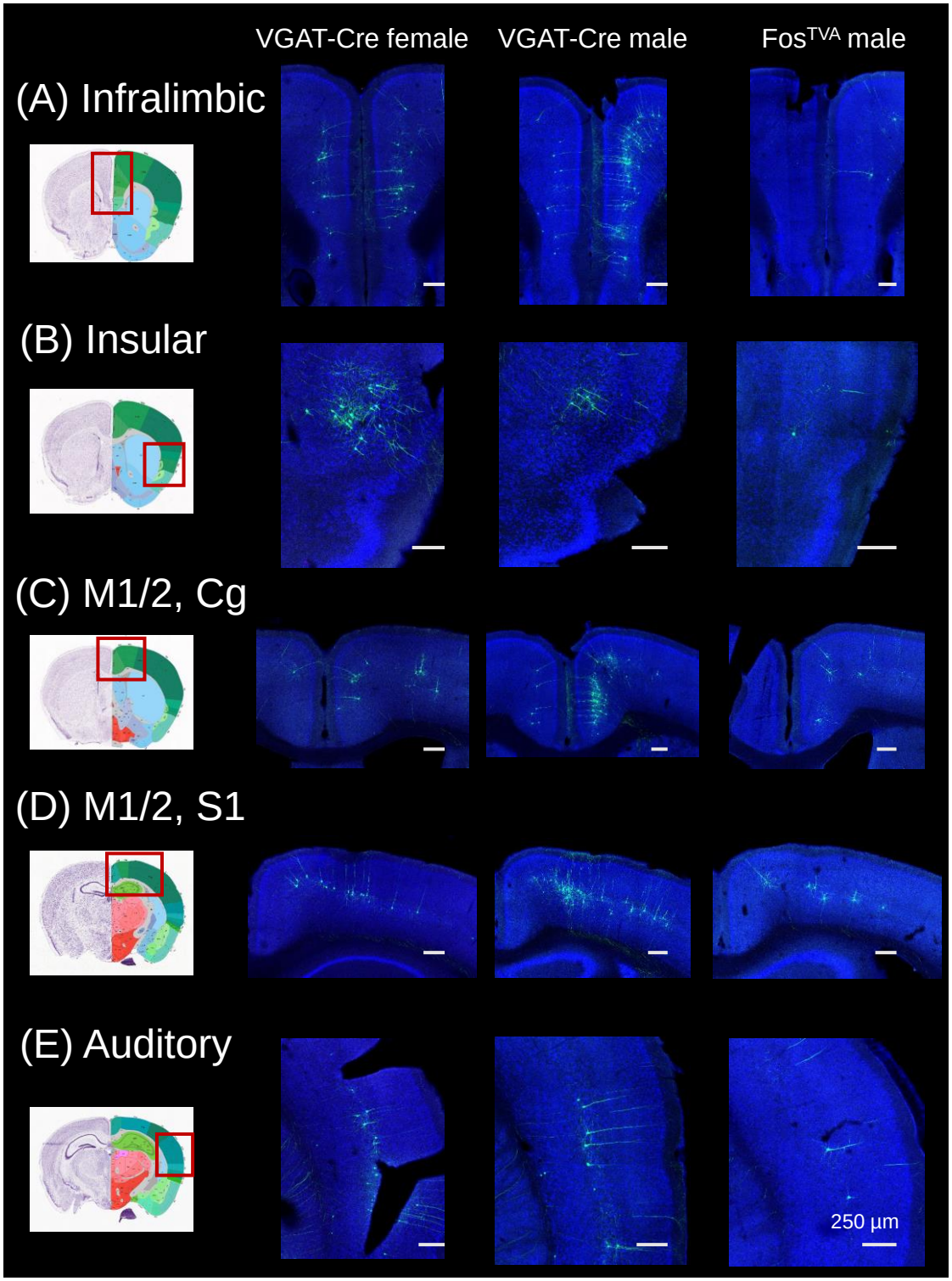

Figure S2, related to Figure 1: Monosynaptic rabies-based tracing reveals cortical inputs to the midbrain vocalization circuit. (A) Example confocal images showing transsynaptic labeling of neurons in the infralimbic cortex (green) that provide monosynaptic input to GABAergic PAG neurons (left-most confocal image, VGAT-Cre female; middle confocal image, VGAT-Cre male) or to PAG-USV neurons (right confocal image, Fos^{TVA} male; blue, Neurotrace). (B-E) Same, for transsynaptically labeled neurons in (B) insular cortex, (C) motor (M1, M2), and cingulate (Cg) cortices, (D) M1, M2, and somatosensory cortex (S1), and (E) auditory cortex. Coronal brain atlas images show the approximate plane of section of the confocal images to the right. Red rectangles superimposed on the atlas images indicate the approximate location of the brain regions shown in the confocal images. See also Table S1 and Figures S1, S3, and S4. Scale bars, 250 µm. All brain atlas images were obtained from the Allen Mouse Brain Reference Atlas, (https://mouse.brain-map.org/experiment/thumbnails/100048576?Image_type=atlas).

Figure S3, related to Figure 1: Monosynaptic rabies-based tracing reveals additional hypothalamic inputs to the midbrain vocalization circuit.

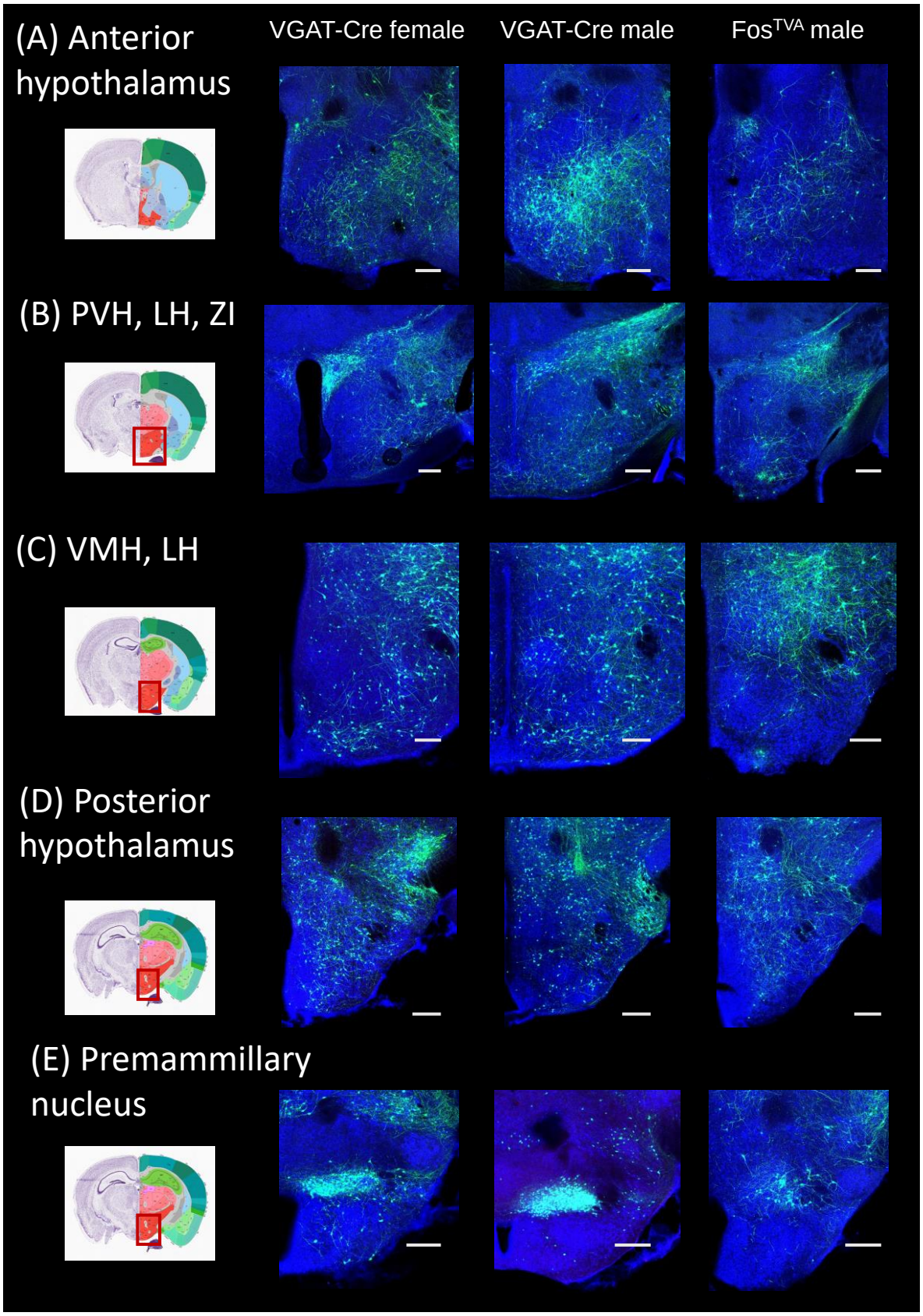

Figure S3, related to Figure 1: Monosynaptic rabies-based tracing reveals additional hypothalamic inputs to the midbrain vocalization circuit. (A) Example confocal images showing transsynaptic labeling of neurons in the anterior hypothalamus (green) that provide monosynaptic input to GABAergic PAG neurons (left-most confocal image, VGAT-Cre female; middle confocal image, VGAT-Cre male) or to PAG-USV neurons (right confocal image, Fos^{TVA} male; blue, Neurotrace). (B-D) Same, for transsynaptically labeled neurons in (B) the paraventricular nucleus (PVN), lateral hypothalamus (LH), and zone incerta (ZI), (C) ventromedial hypothalamus (VMH) and LH, (D) posterior hypothalamus, and (E) premammillary nucleus. Coronal brain atlas images show the approximate plane of section of the confocal images to the right. Red rectangles superimposed on the atlas images indicate the location of the brain regions shown in the confocal images. See also Table S1 and Figures S1, S2, and S4. Scale bars, 250 µm. All brain atlas images were obtained from the Allen Mouse Brain Reference Atlas, (https://mouse.brain-map.org/experiment/thumbnails/100048576?Image_type=atlas).

Figure S4, related to Figure 1: Monosynaptic rabies-based tracing reveals additional subcortical inputs to the midbrain vocalization circuit.

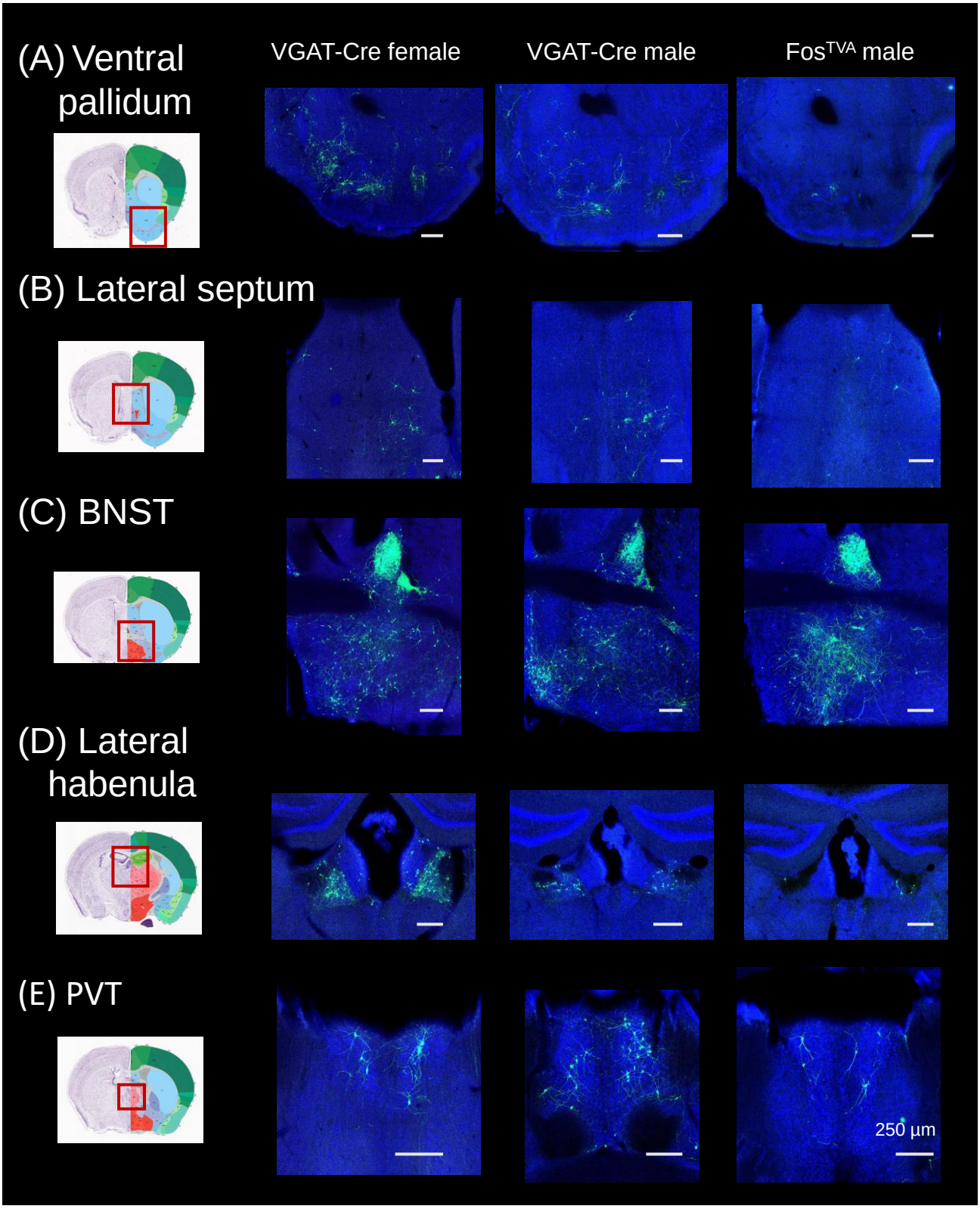

Figure S4, related to Figure 1: Monosynaptic rabies-based tracing reveals additional subcortical inputs to the midbrain vocalization circuit. (A) Example confocal images showing transsynaptic labeling of neurons in the ventral pallidum (green) that provide monosynaptic input to GABAergic PAG neurons (left-most confocal image, VGAT-Cre female; middle confocal image, VGAT-Cre male) or to PAG-USV neurons (right confocal image, Fos^{TVA} male; blue, Neurotrace). (B-D) Same, for transsynaptically labeling of neurons in (B) lateral septum, (C) bed nucleus of the stria terminals (BNST), (D) lateral habenula, and (E) paraventricular nucleus of the thalamus (PVT). Coronal brain atlas images show the approximate plane of section of the confocal images to the right. Red rectangles superimposed on the atlas images indicates the location of the brain regions shown in the confocal images. See also Table S1 and Figures S1-3. Scale bars, 250 µm. All brain atlas images were obtained from the Allen Mouse Brain Reference Atlas, (https://mouse.brain-map.org/experiment/thumbnails/100048576?Image_type=atlas).

Figure S5, related to Figures 2 and 4: Additional information related to the optogenetic activation of POA_{PAG}, POA-Esr1^{+} neurons, and $Amg_{C/M-PAG}$ neurons

A Real-time place preference tests

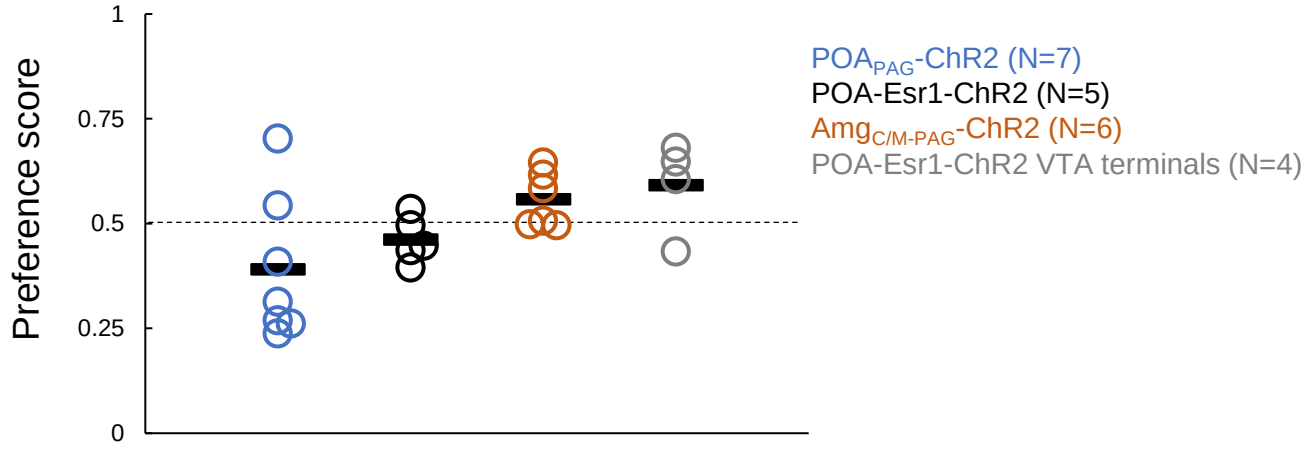

B Effects of optogenetic activation on movement

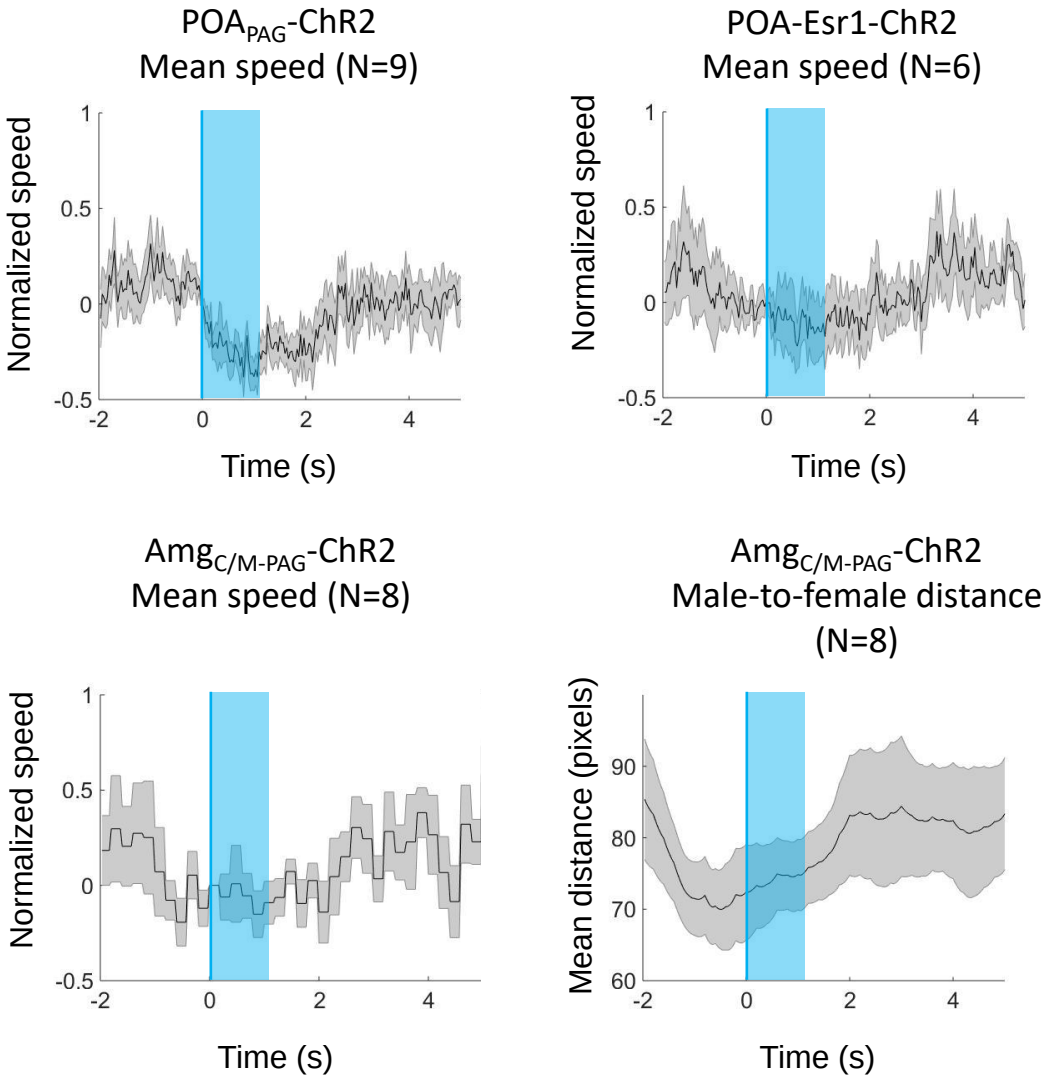

Figure S5, related to Figures 2 and 4. Additional information related to the optogenetic activation of POA_{PAG}, POA-Esr1+ neurons, and $Amg_{C/M-PAG}$ neurons. (A) Real-time place preference tests were performed in which either POA or $Amg_{C/M}$ neurons were optogenetically activated when mice were in one of two sides of a test chamber (see Methods). (B) The mean speeds of mice were calculated and aligned to the onset of optogenetic activation of POA_{PAG} neurons (top left), POA-Esr1^{+} neurons (top right), and $Amg_{C/M-PAG}$ neurons (bottom left). (Bottom, right) Distances between male $Amg_{C/M-PAG}$-ChR2 mice and their female social partners were calculated and aligned to the onset of optogenetic activation of $Amg_{C/M-PAG}$ neurons.

Figure S6, related to Figure 2: Additional characterization of USVs elicited by optogenetic activation of POA neurons

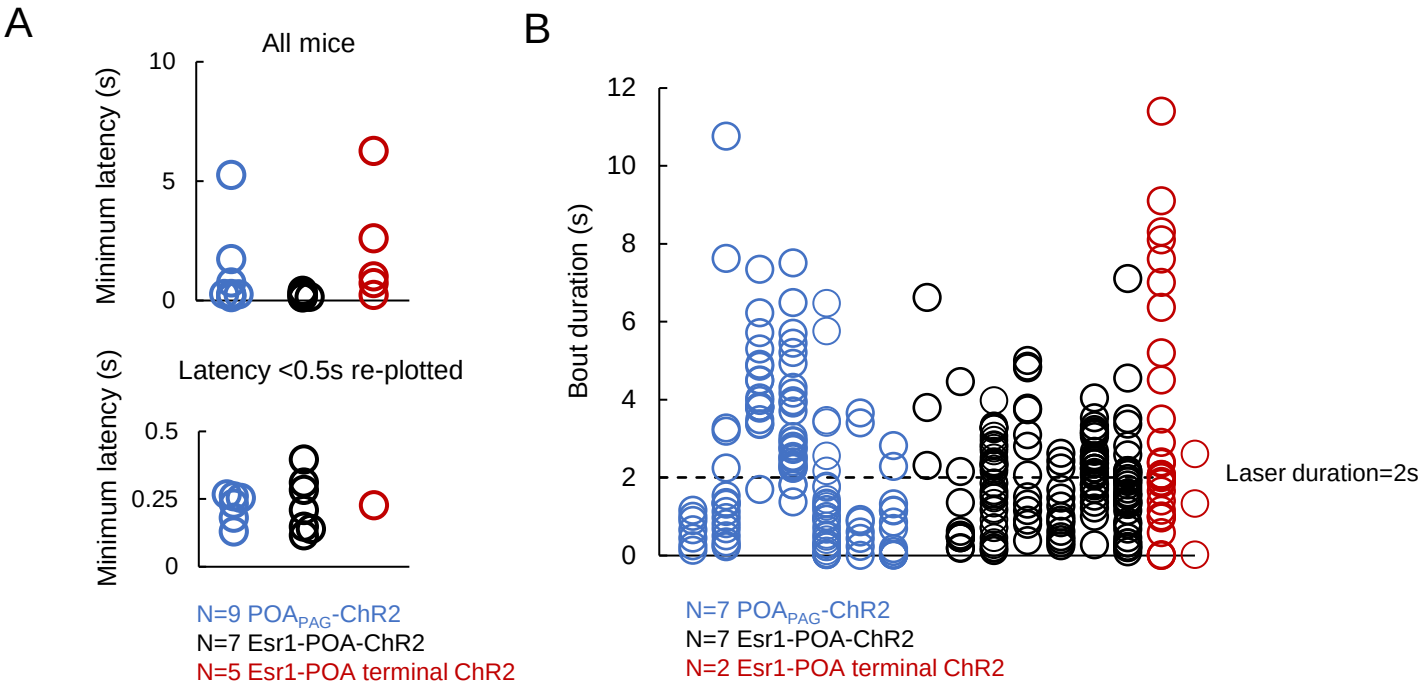

Figure S6, related to Figure 2. Additional characterization of USVs elicited by optogenetic activation of POA neurons. Top: the minimum latency from the onset of optogenetic stimulation to the onset of the first optogenetically-elicited USV is plotted for three groups of mice: ChR2 expressed in POA$_{PAG}$ neurons (N=9 mice, blue points), ChR2 expressed in Esr1^{+} POA neurons (N=7 mice, black points), and ChR2 expressed in axon terminals within the PAG of Esr1^{+} POA neurons (N=5 mice, red points). Bottom: same plot as above, but with the y range restricted from 0 to 0.5s. (B) Quantification of the duration of USV bouts elicited by 2s, 10-20 Hz optogenetic stimulation of POA neurons. Each column represents a different mouse, and each point represents the duration of a USV bout elicited by a 2s-long optogenetic stimulus. Colors as in (A). Please note that 5 animals shown in (A) had only a small number of 2-s long optogenetic activation trials and were therefore not included in the analysis shown in (B).

Figure S7, related to Figure 4: Extent of cell body labeling of $Amg_{C/M\text{-}PAG}$ neurons

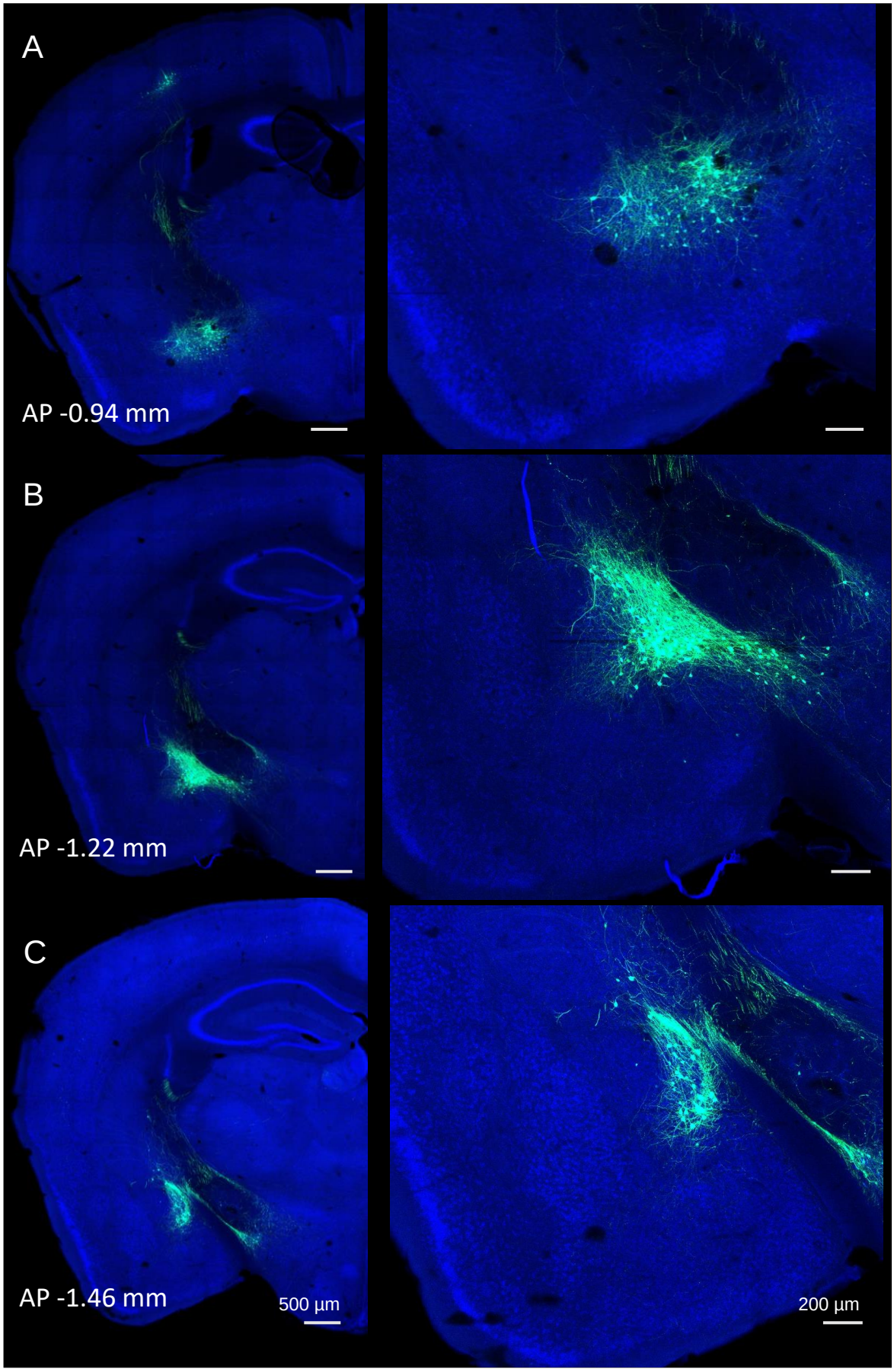

Figure S7, related to Figure 4. Extent of cell body labeling of $Amg_{C/M-PAG}$ neurons. $Amg_{C/M-PAG}$ neurons were labeled by injecting AAV-retro-Cre into the caudolateral PAG and AAV-FLEX-GFP into the $Amg_{C/M}$. (A-C) Three planes of coronal section are shown that cover the rostral to caudal extent of $Amg_{C/M-PAG}$ cell body labeling.

Figure S8, related to Figure 4: Comparison of hypothalamus and amygdala cell body labeling achieved after transsynaptic tracing from the PAG vocal gating circuit versus AAV-retro-Cre injection into the caudolateral PAG

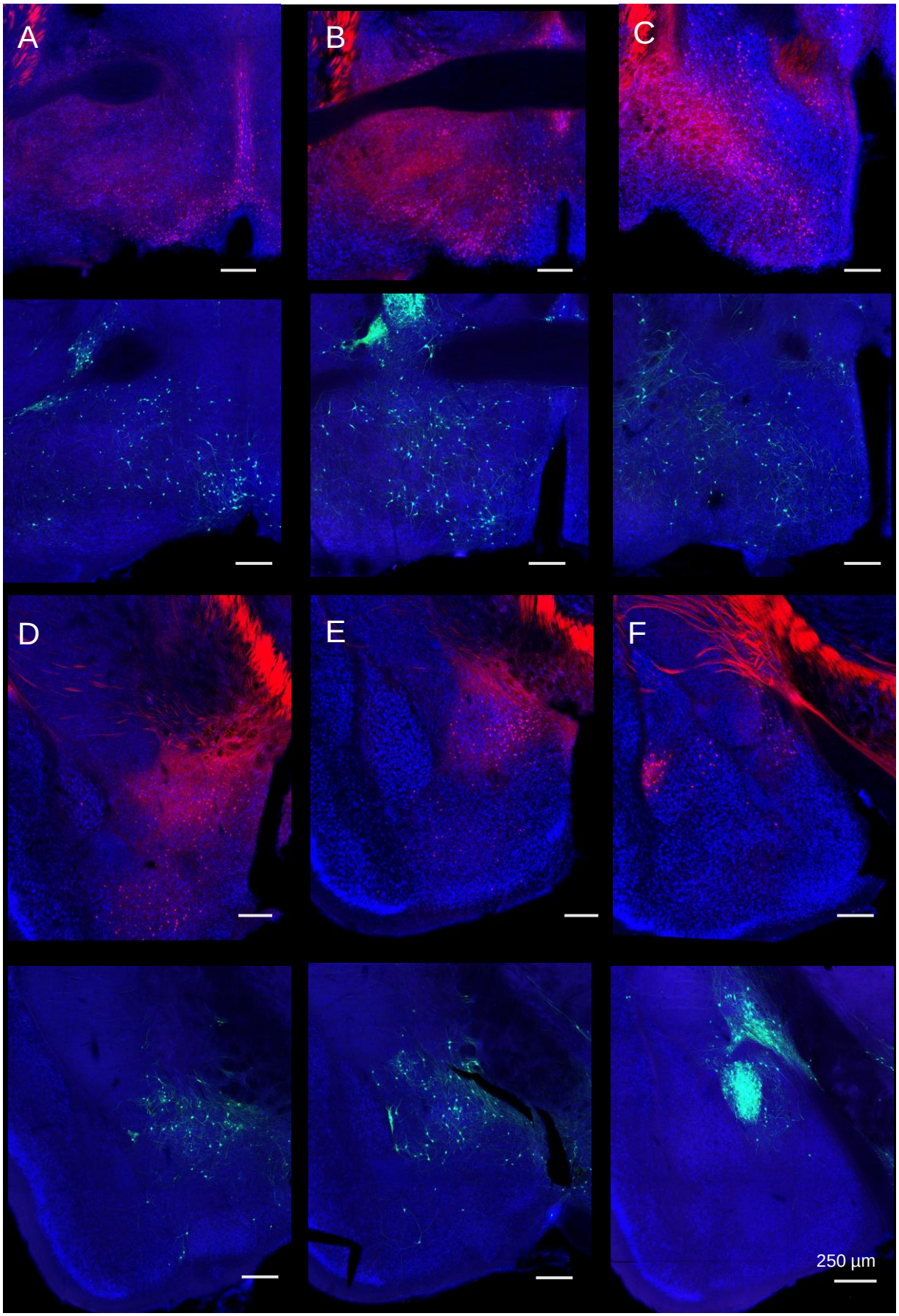

Figure S8, related to Figure 4. Comparison of hypothalamus and amygdala cell body labeling achieved after transsynaptic tracing from the PAG vocal gating circuit versus AAV-retro-Cre injection into the caudolateral PAG. Representative coronal sections are shown for forebrain cell body labeling observed after monosynaptic rabies-based tracing from GABAergic PAG neurons (bottom rows, GFP-labeled cells) or AAV-retro-Cre injection into the caudolateral PAG of an Ai14 reporter mouse (top rows, tdTomato-labeled cells, see Methods). A-F show different planes of section as noted. Note that although both $Amg_{C/M}$ and CeA neurons are labeled after transsynaptic tracing from PAG-GABA neurons (D-F, bottom row), CeA neuronal labeling is absent after injection of AAV-retro-Cre (F, top row). Scale bars, 250 µm.

Figure S9, related to Figures 2 and 4: Dual tracing of the axonal projections of POA_{PAG} and $Amg_{C/M-PAG}$ neurons

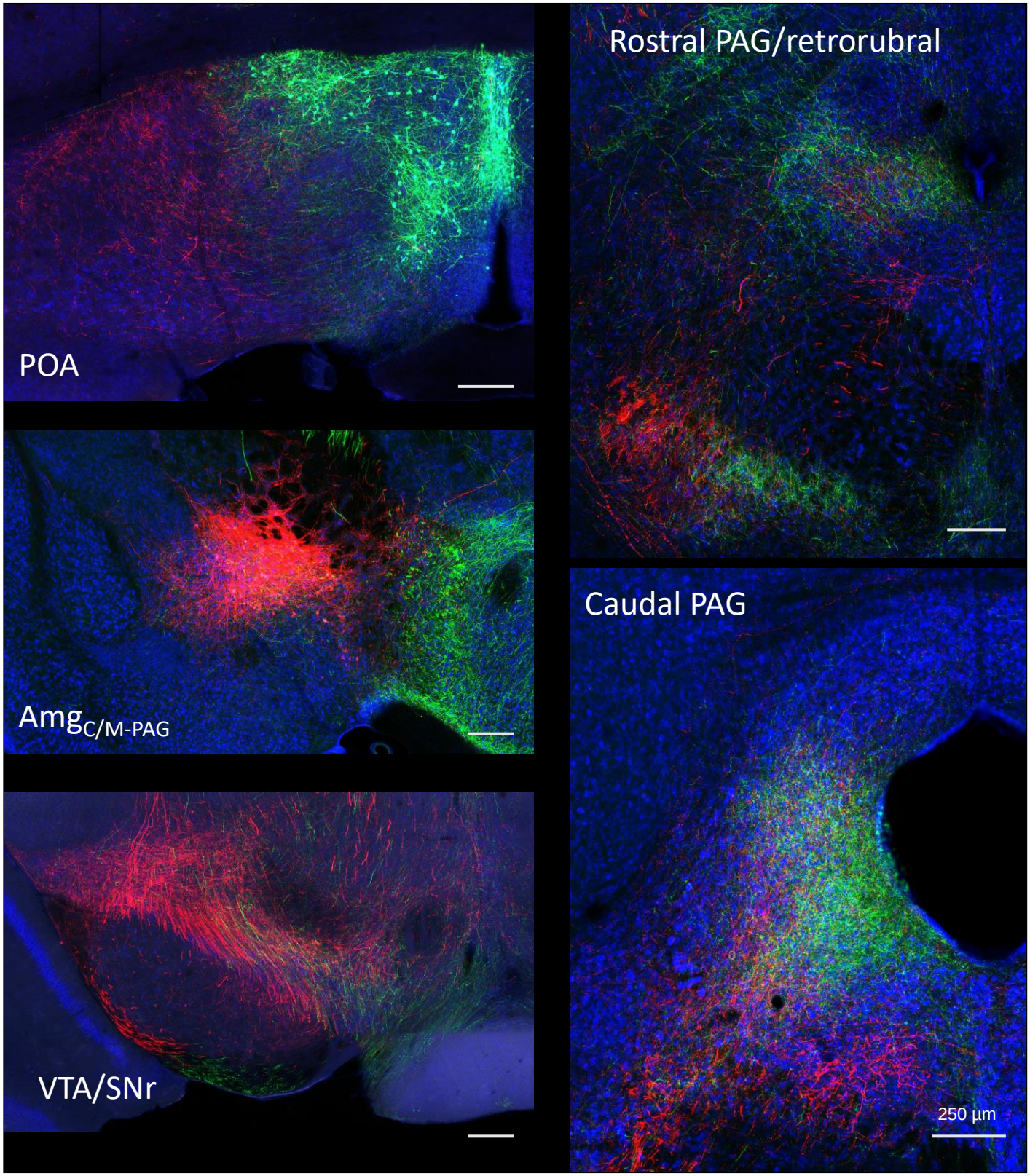

Figure S9, related to Figures 2 and 4. **Dual tracing of the axonal projections of POA_{PAG} and $Amg_{C/M-PAG}$ neurons.** POA_{PAG} neurons are labeled with GFP, and $Amg_{C/M-PAG}$ neurons are labeled with tdTomato. (Top left) Plane of section through the POA shows the beginning of POA_{PAG} cell body labeling in green and axonal projections to the lateral POA from $Amg_{C/M-PAG}$ neurons in red. (Middle left) Plane of section through the $Amg_{C/M-PAG}$ shows axonal projections from POA_{PAG} neurons that overlap with $Amg_{C/M-PAG}$ cell bodies. (Bottom left) Plane of section through the VTA/SNr. (Top right) Plane of section including the rostral PAG and retrorubral area. (Bottom right) Place of section through the caudal PAG, showing the overlapping terminal fields of POA_{PAG} and $Amg_{C/M-PAG}$ neurons. These representative images are from a female mouse, and we found that POA_{PAG} and $Amg_{C/M-PAG}$ neurons have similar axonal projections in males and females (data not shown).

Figure S10, related to Figure 6: POA neurons provide direct inhibition onto few PAG-USV neurons

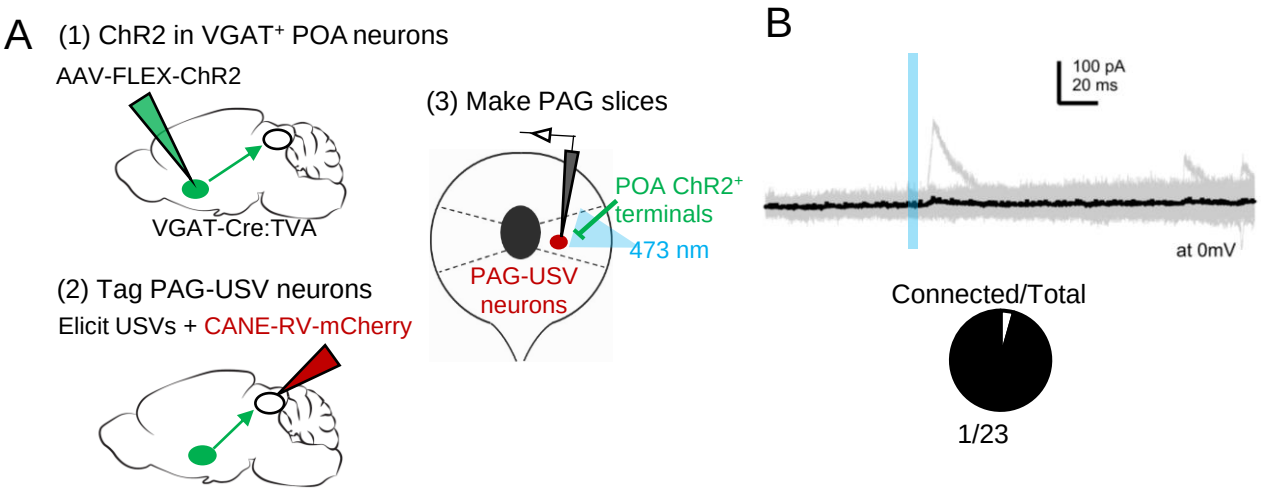

Figure S10, related to Figure 6. **POA neurons provide direct inhibition onto few PAG-USV neurons.** (A) Viral strategy (left) and schematic (right) for whole-cell patch clamp recordings from fluorescently identified PAG-USV cells while optogenetically activating POA_{PAG} axons. (B) Light-evoked IPSCs were observed in 1 of 23 mCherry-labeled PAG-USV neurons recorded from 7 mice.

Movie S1, related to Figure 2. Optogenetic activation of POA_{PAG} neurons elicits USVs. An isolated male mouse is shown which has ChR2 is expressed in POA_{PAG} neurons. Optogenetic activation of these neurons with pulses of blue light elicits USV production. Video is shown at the top, a spectrogram (bottom) showing the optogenetically-elicited USVs is synchronized to the video, and pitch-shifted audio (80 kHz to 5 kHz transformation) is included to place the USVs within the human hearing range.

Movie S2, related to Figure 4. Optogenetic activation of $Amg_{C/M\text{-}PAG}$ neurons transiently suppresses USV production. A male mouse which has ChR2 expressed in $Amg_{C/M\text{-}PAG}$ neurons is shown interacting with and producing USVs directed at a female social partner. Optogenetic activation of these neurons with pulses of blue light transiently suppresses USV production without suppressing non-vocal courtship behavior. Video is shown at the top, a spectrogram (bottom) showing the optogenetically-elicited USVs is synchronized to the video, and pitch-shifted audio (80 kHz to 5 kHz transformation) is included to place the USVs within the human hearing range.

Table S1, related to Figure 1. List of forebrain inputs to the PAG vocal gating circuit.

Cortical regions	VGAT+ PAG	PAG-USV
Prelimbic/infralimbic	+	+
Insular	+	+
M1/M2	+	+
Cingulate	+	+
S1/S2	+	+
Auditory	+	+
Subcortical	VGAT+ PAG	PAG-USV
Ventral pallidum	+	+
Lateral septum	+	+
BNST	+	+
Habenula	+	+
Zona incerta	+	+
Hypothalamus	VGAT+ PAG	PAG-USV
Preoptic	+	+
Anterior hypothalamus	+	+
Lateral hypothalamus	+	+
PVH	+	+
VMH	+	+
Posterior hypothalamus	+	+
Premammillary/mammillary	+	+
Amygdala	VGAT+ PAG	PAG-USV
Central-medial boundary	+	+
Central amygdala	+	+
Thalamus	VGAT+ PAG	PAG-USV
PVT	+	+